

U.S. DEPARTMENT OF COMMERCE  
National Technical Information Service

AD-A032 412

TELESEISMIC VERIFICATION OF  
DATA EXCHANGE YIELDS

SYSTEMS, SCIENCE AND SOFTWARE,  
LA JOLLA, CALIFORNIA

MAY 1976

AD A032412

334108



**SYSTEMS, SCIENCE AND SOFTWARE**

SSS-R-76-2941

**TELESEISMIC VERIFICATION OF DATA EXCHANGE YIELDS**

T. C. Bache  
T. G. Barker  
J. T. Cherry  
J. M. Savino

Topical Report

Sponsored by  
Advanced Research Projects Agency  
ARPA Order No. 2551



This research was supported by the Advanced Research Projects Agency of the Department of Defense and was monitored by AFTAC/VSC, Patrick AFB FL 32929, under Contract No. F08606-75-C-0045.

The views and conclusions contained in this document are those of the authors and should not be interpreted as necessarily representing the official policies, either expressed or implied, of the Advanced Research Projects Agency, the Air Force Technical Applications Center, or the U. S. Government.

Approved for Public Release, Distribution Unlimited

May 1976

P. O. BOX 1620, LA JOLLA, CALIFORNIA 92038, TELEPHONE (714) 453-0060

REPRODUCED BY  
**NATIONAL TECHNICAL  
INFORMATION SERVICE**  
U. S. DEPARTMENT OF COMMERCE  
SPRINGFIELD, VA. 22161

AFTAC Project Authorization No. VELA T/6712/B/ETR

Program Code No. 6F10

Effective Date of Contract: May 1, 1975

Contract No. F08606-75-C-0045

Principal Investigator and Phone No.

Dr. John M. Savino, (714) 453-0060

Project Scientist and Phone No.

Dr. Ralph W. Alewine, III, (202) 325-8484

1a

UNCLASSIFIED

SECURITY CLASSIFICATION OF THIS PAGE (When Data Entered)

REPORT DOCUMENTATION PAGE		READ INSTRUCTIONS BEFORE COMPLETING FORM
1. REPORT NUMBER	2. GOVT ACCESSION NO.	3. RECIPIENT'S CATALOG NUMBER
4. TITLE (and Subtitle) TELESEISMIC VERIFICATION OF DATA EXCHANGE YIELDS		5. TYPE OF REPORT & PERIOD COVERED Topical Report
		6. PERFORMING ORG. REPORT NUMBER SSS-R-76-2941
7. AUTHOR(s) T. C. Bache, T. G. Barker, J. T. Cherry and J. M. Savino		8. CONTRACT OR GRANT NUMBER(s) Contract No. F08606-75-C-0045
9. PERFORMING ORGANIZATION NAME AND ADDRESS Systems, Science and Software P. O. Box 1620 La Jolla, CA 92038		10. PROGRAM ELEMENT, PROJECT, TASK AREA & WORK UNIT NUMBERS Program Code No. 6F10 ARPA Order No. 2551
11. CONTROLLING OFFICE NAME AND ADDRESS VELA Seismological Center 312 Montgomery Street Alexandria, Virginia 22314		12. REPORT DATE May 1976
		13. NUMBER OF PAGES 61
14. MONITORING AGENCY NAME & ADDRESS (if different from Controlling Office)		15. SECURITY CLASS. (of this report) Unclassified
		15a. DECLASSIFICATION/DOWNGRADING SCHEDULE
16. DISTRIBUTION STATEMENT (of this Report) Approved for Public Release, Distribution Unlimited		
17. DISTRIBUTION STATEMENT (of the abstract entered in Block 20, if different from Report)		
18. SUPPLEMENTARY NOTES		
19. KEY WORDS (Continue on reverse side if necessary and identify by block number) Explosion Seismology                      Ground Motion Seismic Yields Explosion Source Functions Earth Structure		
20. ABSTRACT (Continue on reverse side if necessary and identify by block number) This report addresses the possibility of directly inverting teleseismic ground motion in order to obtain explosion yield. The procedure proposed for accomplishing the inversion is to employ a deterministic model which predicts ground motion from a nuclear explosion. This procedure makes use of the information expected from data exchange packages that provide information on the near explosion source environment. Additional parameters must be inferred from other sources or determined by experiment on geophysical analogues.		

DD FORM 1 JAN 73 1473

EDITION OF 1 NOV 65 IS OBSOLETE

UNCLASSIFIED

1

SECURITY CLASSIFICATION OF THIS PAGE (When Data Entered)

UNCLASSIFIED

SECURITY CLASSIFICATION OF THIS PAGE(When Data Entered)

Three major topics discussed in this report are: equivalent elastic source calculations for a wide range of rock types; the teleseismic amplitude dependence on the source, including the effects of the free surface reflected phase, pP, and the effect of upper mantle elastic properties on short period P waves.

ACCESSION for	
NTIS	White Section <input checked="" type="checkbox"/>
DDC	Buff. Section <input type="checkbox"/>
UNANNOUNCED	<input type="checkbox"/>
JUSTIFICATION	
BY	
DISTRIBUTION AVAILABILITY CODES	
Dist.	AVAIL. and/or SPECIAL
A	

UNCLASSIFIED

SECURITY CLASSIFICATION OF THIS PAGE(When Data Entered)

## TABLE OF CONTENTS

	Page
I. INTRODUCTION . . . . .	1
II. THE EQUIVALENT ELASTIC SOURCE . . . . .	3
III. TELESEISMIC AMPLITUDE DEPENDENCE OF THE SOURCE . . . . .	9
IV. BODY WAVE AMPLITUDE CORRECTION FOR pP . . . . .	22
V. MAGNITUDE-YIELD SCALING INCLUDING CORRECTIONS FOR DEPTH OF BURIAL . . . . .	32
VI. TWO "ANOMALOUS" EVENTS; FAULTLESS AND A FRENCH EXPLOSION AT THE HOGGAR TEST SITE . . . . .	38
VII. EFFECT OF THE UPPER MANTLE ELASTIC PROPERTIES ON SHORT PERIOD SEISMOGRAMS . . . . .	46
REFERENCES . . . . .	54

## I. INTRODUCTION

This working paper addresses the possibility of directly inverting teleseismic ground motion in order to obtain explosion yield. We propose to accomplish this inversion via a deterministic model which predicts the teleseismic ground motion for a nuclear explosion.

A schematic of the model is shown in Figure 1.1. It is the explosion yield, which controls the amplitude of the equivalent elastic source, that we wish to obtain based on a comparison between the predicted and observed ground motion.

Obviously this approach is nonsense unless the remaining key parameters in the model are known. For a given receiver structure and instrument response the key parameters are as follows:

1. The material properties and constitutive model of the near source rock environment.
2. The pP delay times.
3. The anelastic properties of the earth's upper mantle.

What can we learn from the data exchange? Our intent is to use the data to choose an analog rock whose material properties are consistent with the data furnished in the exchange. This provides enough information to permit an a priori calculation of the equivalent source.

If we can determine the equivalent source for the near source rock environment, then the pP delay time and the anelastic properties of the earth's upper mantle required by our model may be found from the details of the recorded ground motion.



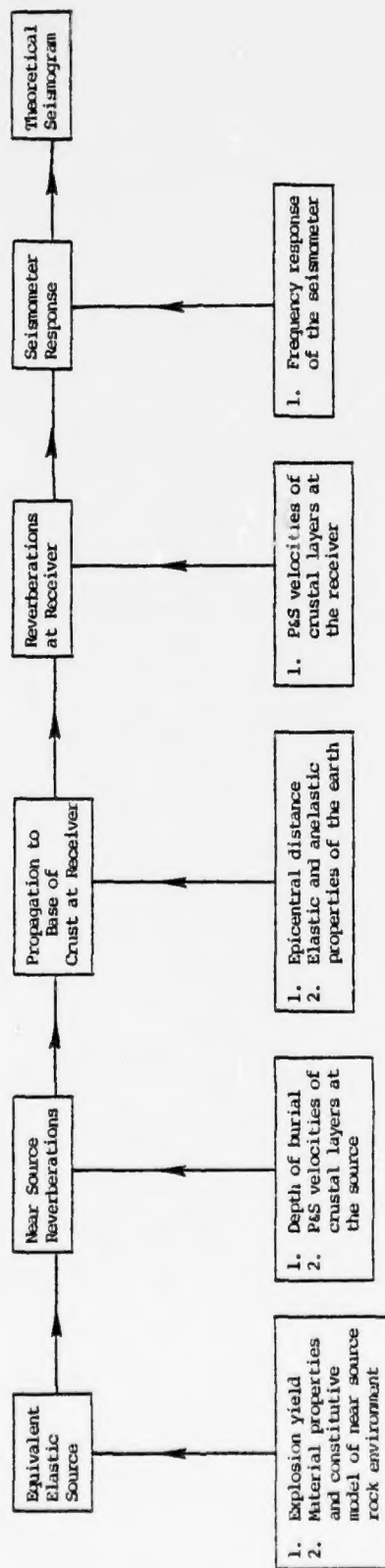


Figure 1.1. Schematic representation for the deterministic prediction of the teleseismic ground motion from a nuclear explosion.



## II. THE EQUIVALENT ELASTIC SOURCE

Figures 2.1 and 2.2 show the calculated far-field displacement spectra of the indicated rock types. In all cases the device yield was 150 kt and the DOB equaled 1860 ft ( $350 W^{1/3}$ ). Table 1 lists the material properties used for each calculation. The shot name for the event located in each material is also given in the table. We should note that measured material properties were used in the source calculations. These sources, when used in conjunction with the model in Figure 1.1, explain both the free-field and tele-seismic data available to us.

Since there is a factor of ten difference in amplitude at 1 Hz between the maximum and minimum source functions, it is important to subdivide these sources into classes. Table 2 performs this separation. Figure 2.3 shows the source functions for all rock types except Class I (207) and illustrates the natural decomposition of sources into their respective classes. It is our intention to use the information from the data exchange to:

1. Classify the near source rock environment.
2. Perturb the material properties in the class to fit the given depth of burial, density, P wave velocity and, hopefully, S wave velocity.
3. Calculate the range of equivalent sources which are possible in this class. This range will include reasonable variations in material strength and air-filled porosity consistent with past experience from similar rock types.

SOURCES 201-207 AT 150 KT

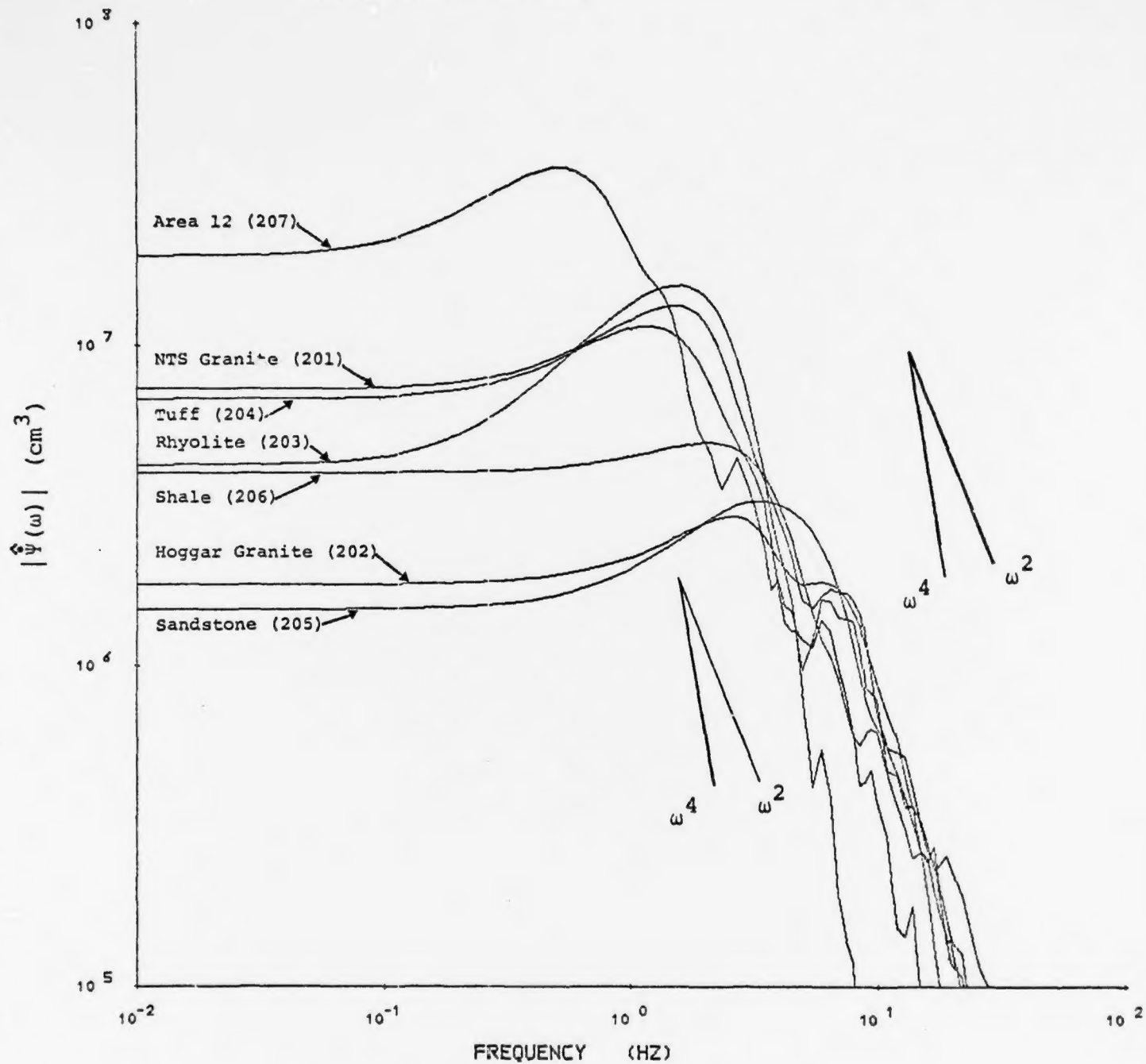


Figure 2.1. Source functions for indicated rock types.

SOURCES 201-207 AT 150 KT

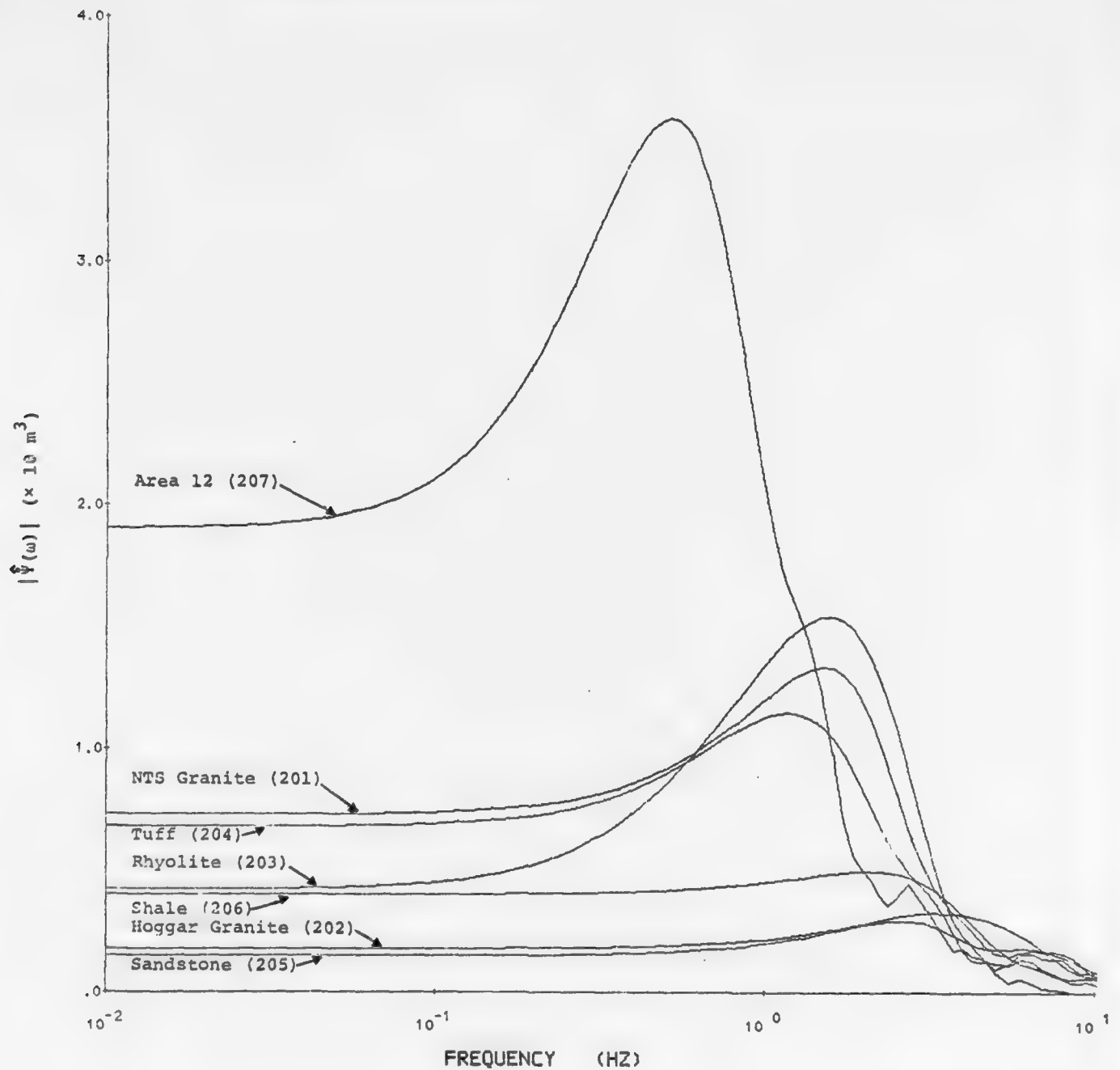


Figure 2.2. Source functions for indicated rock types.

TABLE 1

$\rho$	$\alpha$	$\mu$	$\gamma_0$	$\gamma_m$	$\bar{P}_m$	$P_0$	Rock Type	Shot Name	Calc	Water Content
2.67	5.33	207	0.3	7.7	9	148	NTS Granite	PILED RIVER	201	Saturated
							Hoggar	F	202	Dry
2.45	4.2	169	0.3	7.7	9	136	Rhyolite	MAST	203	Saturated
2.2	3.07	90	0.15	3.85	9	122	Tuff (PM)	KASSERI	204	Saturated
2.51	4.28	204	0.2	11.8	12	140	Sandstone } Shale }	GB	205	Dry
2.61	3.87	147	0.2	3.8	8	145			206	Dry
1.94	2.42	40	0.05	0.35	2	106	Tuff (A-12)	DNA	207	Saturated

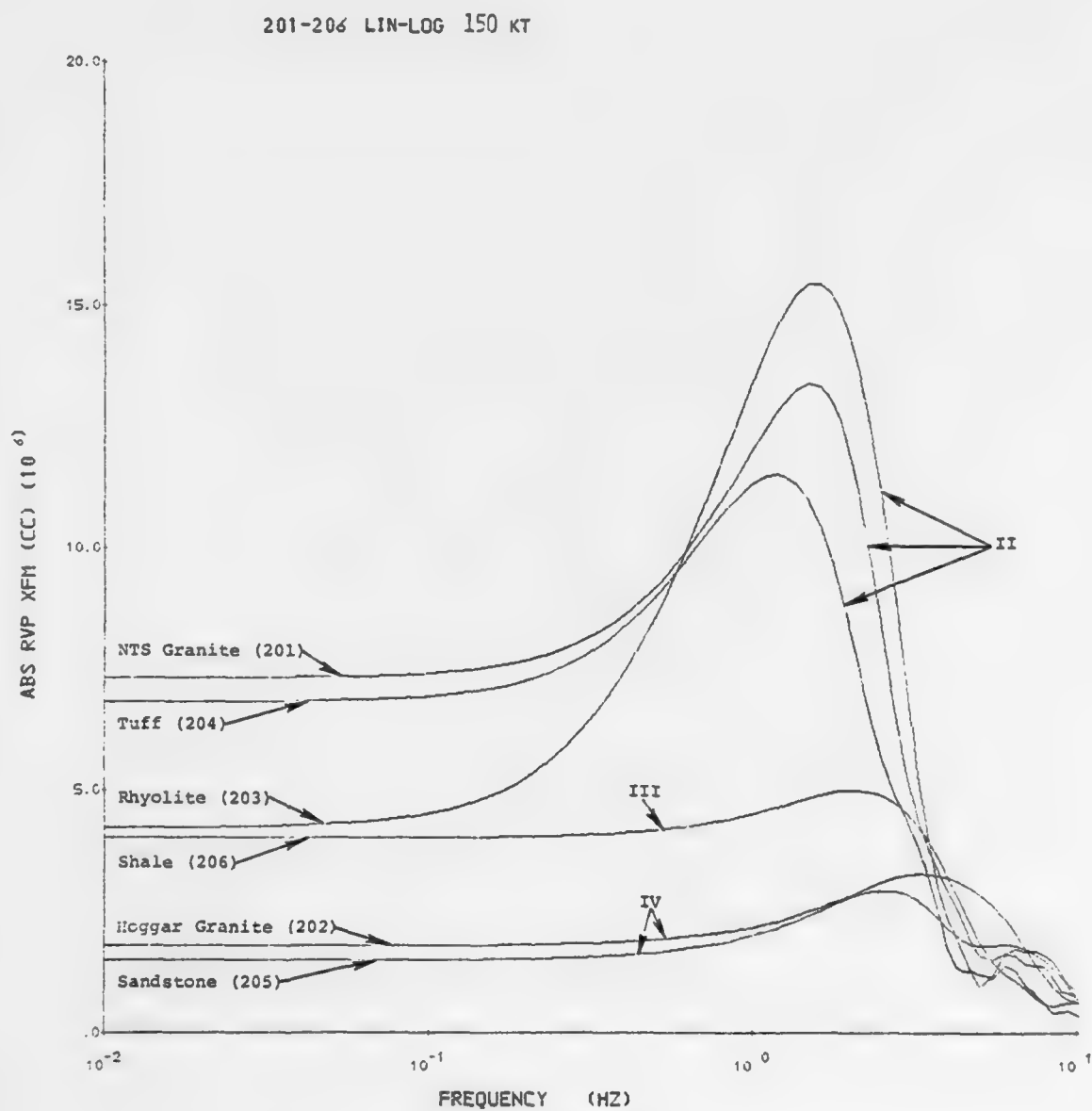


Figure 2.3. Source functions for all rock types except 207.

TABLE 2

<u>Calculation</u>	<u>Class</u>	<u>Description</u>	<u>Rock Type</u>	<u><math>\alpha</math></u>	<u><math>\mu</math></u>	<u><math>\hat{\Psi}</math> (1.0)</u>
207	I	Weak, saturated	Tuff	2.4	40	19
201	II	Strong, saturated	Granite	5.3	207	12.0
203	II	Strong, saturated	Rhyolite	4.2	170	15.3
204	II	Strong, saturated	Tuff	3.1	90	11.2
206	III	Weak, dry	Shale	3.9	150	4.6
202	IV	Strong, dry	Granite	5.3	207	2.5
205	IV	Strong, dry	Sandstone	4.3	204	2.0

### III. TELESEISMIC AMPLITUDE DEPENDENCE ON THE SOURCE

The fundamental output of our nonlinear finite difference calculations is the reduced displacement potential ( $\Psi(\tau)$ ) representation of the explosion source. In Figure 2.1 we plotted  $|\hat{\Psi}(\omega)|$  for seven 150 kt explosion detonated in a representative range of emplacement materials. These source spectra span a considerable range of amplitudes and spectral shapes. How do the source spectra translate into short period seismogram amplitudes at teleseismic ranges; that is, into  $m_b$ ? The relation between the two is discussed in this section.

In a homogeneous space, the displacement is related to the reduced displacement potential in the frequency domain by

$$\hat{u}_s = \left( \frac{\hat{\Psi}(\omega)}{R\alpha} + \frac{\hat{\Psi}(\omega)}{R^2} \right) e^{-ik_\alpha R}, \quad (3.1)$$

where  $k_\alpha = \omega/\alpha$ . In the far-field the  $R^{-1}$  term dominates. The vertical component of the teleseismic ground motion is then related to the source region displacement through a series of transfer functions. The relation may be written

$$\hat{u}_R = \hat{u}_S \cdot T_S(\omega) \cdot T_R(\omega) \cdot T_M(\omega) \cdot I(\omega), \quad (3.2)$$

where

$T_S(\omega)$  - the influence of the crust in the source region,

$T_R(\omega)$  - the influence of the crust in the receiver region,

$T_M(\omega)$  - the influence of the upper mantle,

$I(\omega)$  - the seismograph response.



The transfer functions representing the effect of the earth's crust and upper mantle may be quite complex. Here we shall isolate the source effect by considering only the most elementary forms for these transfer functions.

Assume that the upper mantle transfer function takes the following form:

$$T_M(\omega) = T_{GS} e^{-f\pi T/Q} \quad (3.3)$$

where  $T_{GS}$  is the effective 1/R or geometric spreading factor for the upper mantle path. The  $T/Q$  is taken to be a constant characterising the path.\* For the  $T_R(\omega)$  we simply use a constant ( $a_R$ ) which converts the emerging body waves to vertical motion at the free surface. Then (3.2) reduces to

$$\hat{u}_R = a_R T_{GS} I(\omega) T_S(\omega) \frac{\hat{\psi}(\omega)}{\alpha} e^{-\pi f T/Q}, \quad (3.4)$$

and synthetic seismograms may be computed by transforming  $\hat{u}_R$  to the time domain.

We now specify the common factors ( $a_R$ ,  $T_{GS}$ ,  $I(\omega)$ ,  $T/Q$ ) and compute synthetic seismograms for the range of source functions represented in Figure 2.1. The relative amplitude and frequency content of these seismograms will be dependent only on the character of the source and source crustal structure. Seismograms are computed for four cases of increasing complexity:

---

\* A complex exponential representing the dispersion due to  $Q$  (Strick, 1970) is also included in the calculations but is left out of the formula for clarity.

1. The source region crust is a homogeneous material of the source material. That is,  $T_S(\omega) = 1$ .
2. A different layered earth model represents the crust for each source. The top layer is a halfspace of the source material. That is, there is no free surface. A few kilometers below the source all crustal models are the same. Between the source and this depth a few layers are inserted to represent a fairly smooth increase in velocity with depth.
3. The same structures are used as in 2 but now a free surface is introduced in such a way as to fix the delay time between the direct (P) and free surface reflected (pP) waves. That is, the burial depth is inversely proportional to the  $\alpha$  for the source material. (A small correction is required to account for differences in the takeoff angle.)
4. Calculations like 3 are carried out but now with depth held constant. Then the P-pP lag time is inversely proportional to  $\alpha$ .

The method used to compute  $T_S(\omega)$  for the latter two cases is essentially identical to that developed by Fuchs (1966). This method has been generalized to more complex sources by Bache and Harkrider (1976) and the actual implementation is as outlined there. For the first two cases listed above, the Haskell matrix formulation was modified to allow the first layer to be a halfspace rather than having a free surface (unpublished work).

The common factors for the synthetic seismogram calculations are as follows:

$$a_R = 1.7,$$

$$T_{GS} = 0.95 \times 10^{-4} \text{ (a typical value for distances like 4000 km),}$$

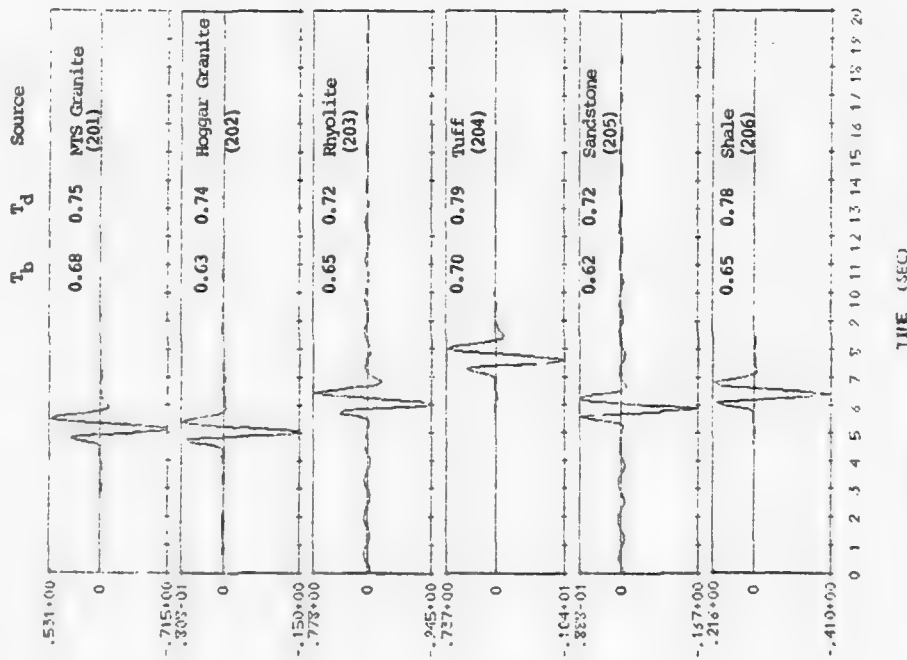
$$T/Q = 0.7 \text{ (perhaps a typical value for Eurasian travel paths).}$$

For the instrument we took response curves provided by the VSC Project Officer, but these are not substantially different from LRSM nominal curves. All calculations are done at a yield of 150 kt.

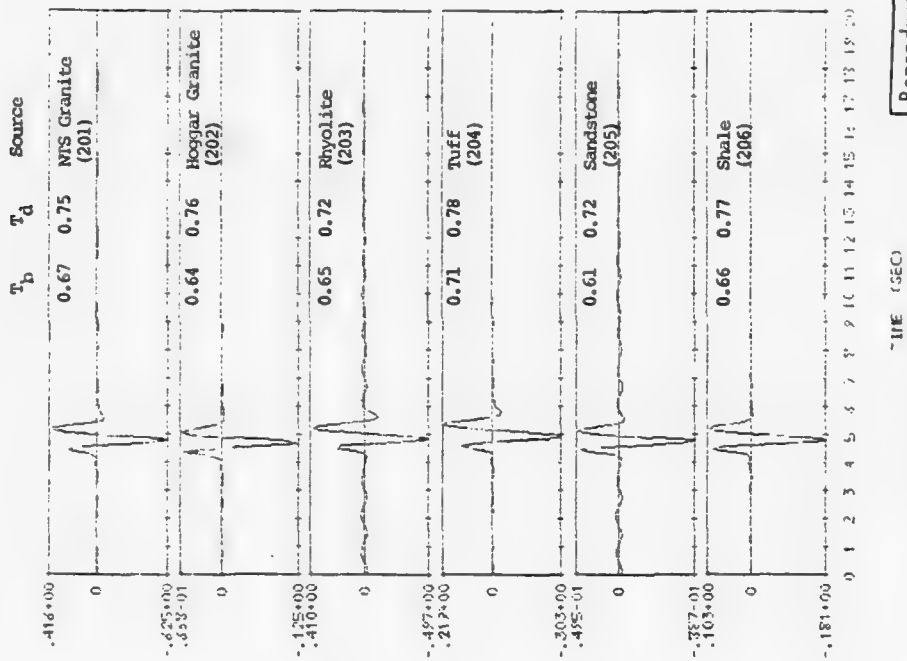
The seismograms for cases 1 and 2 are shown in Figure 3.1. Case 1 is the simplest. Essentially, we are taking the far-field term from the whole space equation (3.1) and transforming to the time domain. We also include the modification by a realistic  $Q$  and a typical instrument. Thus, the seismograms in Figure 3.1a represent the direct P wave, unmodified by any layering effect. Parenthetically, we point out that the source displacement was computed at  $\approx 20$  km from the source, accounting for the travel time differences apparent in the figure.

The source material is different for each of the seismograms of Figure 3.1a. While the material in the source vicinity may vary over the range of materials represented, we suppose that at some depth the underlying rocks are pretty much the same. The direct P wave will certainly be affected by variations in the impedance mismatch between the source material and the underlying common geology.

In computing the seismograms of Figure 3.1b we assumed a different crustal model for each source. These models are tabulated in Table 3. We see that these are very simple crustal models with the source material occurring in a top layer 1.3 km thick. This is underlain by crustal granite. For all the calculations a horizontal phase velocity,  $c = 12.69$  km/sec, was assumed. This translates into a take-off angle of  $28.2^\circ$  at the base of the crust. The takeoff angle at the source is found by applying Snells' law; that is,  $\theta = \sin^{-1} \alpha/c$ .



a. Homogeneous source crust



b. Layered source crust

Figure 3.1. Synthetic seismograms for the direct P wave, Cases 1 and 2 described in the text. The seismograms were computed for the six sources indicated and the yield is 150 kt. There is no free surface in the calculation. The period of the first (b) and second (d) cycles on the record is indicated. The numbers at the left on these and subsequent synthetic seismograms are amplitudes in microns at one Hertz.

Reproduced from  
best available copy.

In summary, the seismograms of Figure 3.1 are for the direct P wave; first, including no layering effects and second, including the propagation from the source material into the underlying common geology. From each of the seismograms we make amplitude measurements in the standard way; that is, we measure a peak-to-peak amplitude and time for both the b and d phases. The periods  $T_b$  and  $T_d$  are then twice the peak-to-peak time and the amplitude is corrected for the instrument response at this period.

How do the amplitudes scale with the source material? For case 1 it is immediately clear that each frequency component of  $\hat{u}_R(\omega)$  scales with  $|\hat{\psi}(\omega)|/\alpha$ . All other factors are held constant in the calculation. The only question is then how much the phase of the spectrum, the Q effect, the instrument and the measuring procedure itself obscure this scaling relationship.

When layering is introduced, the scaling is not so obvious. Bache, et al. (1975, Appendix A) show that in this case  $\hat{u}_R(\omega)$  scales with  $\alpha|\hat{\psi}(\omega)|$ . In brief, the argument is that the far-field term in the whole space equation (3.1) is replaced by

$$|\hat{u}_S| = \frac{A}{L} \frac{|\hat{\psi}(\omega)|}{\alpha} \quad (3.5)$$

where  $\hat{u}_S(\omega)$  is now the displacement spectrum in the common material underlying all the source materials. The A is the reflection coefficients and L replaces R and represents the spreading. Bache, et al. (1975) show that  $A \approx \alpha/\alpha_b$  and  $L \approx \alpha_b/\alpha$  where  $\alpha_b$  is the P wave velocity of the common material. It then follows that  $\hat{u}_S(\omega)$ , and therefore  $\hat{u}_R(\omega)$ , scale with  $\alpha|\hat{\psi}(\omega)|$ .

From the  $T_b$  and  $T_d$  values given in Figure 3.1 we see that the dominant frequency for both the b and d phases is

TABLE 3  
CRUSTAL MODELS FOR SOURCES 201-206

<u>Layer</u>	<u>Depth (km)</u>	<u>Thickness (km)</u>	<u><math>\alpha</math> (km/sec)</u>	<u><math>\beta</math> (km/sec)</u>	<u><math>\rho</math> (g/cm<sup>3</sup>)</u>
*** Sources 201 - 202 ***					
1	1.3	1.3	5.33	2.78	2.67
2	4.1	2.8	5.80	3.45	2.80
3	20.0	15.9	6.0	3.50	2.80
*** Source 203 ***					
1	1.3	1.3	4.20	2.63	2.45
2	2.0	0.7	4.7	2.70	2.60
3	2.7	0.7	5.4	2.80	2.70
4	4.0	1.3	5.8	3.45	2.80
5	20.0	16.0	6.0	3.50	2.80
*** Source 204 ***					
1	1.3	1.3	3.11	2.02	2.2
2-5	As in crust for Source 203				
*** Source 205 ***					
1	1.3	1.3	4.28	2.85	2.51
2-5	As in crust for Source 203				
*** Source 206 ***					
1	1.3	1.3	3.87	2.37	2.61
2-5	As in crust for Source 203				

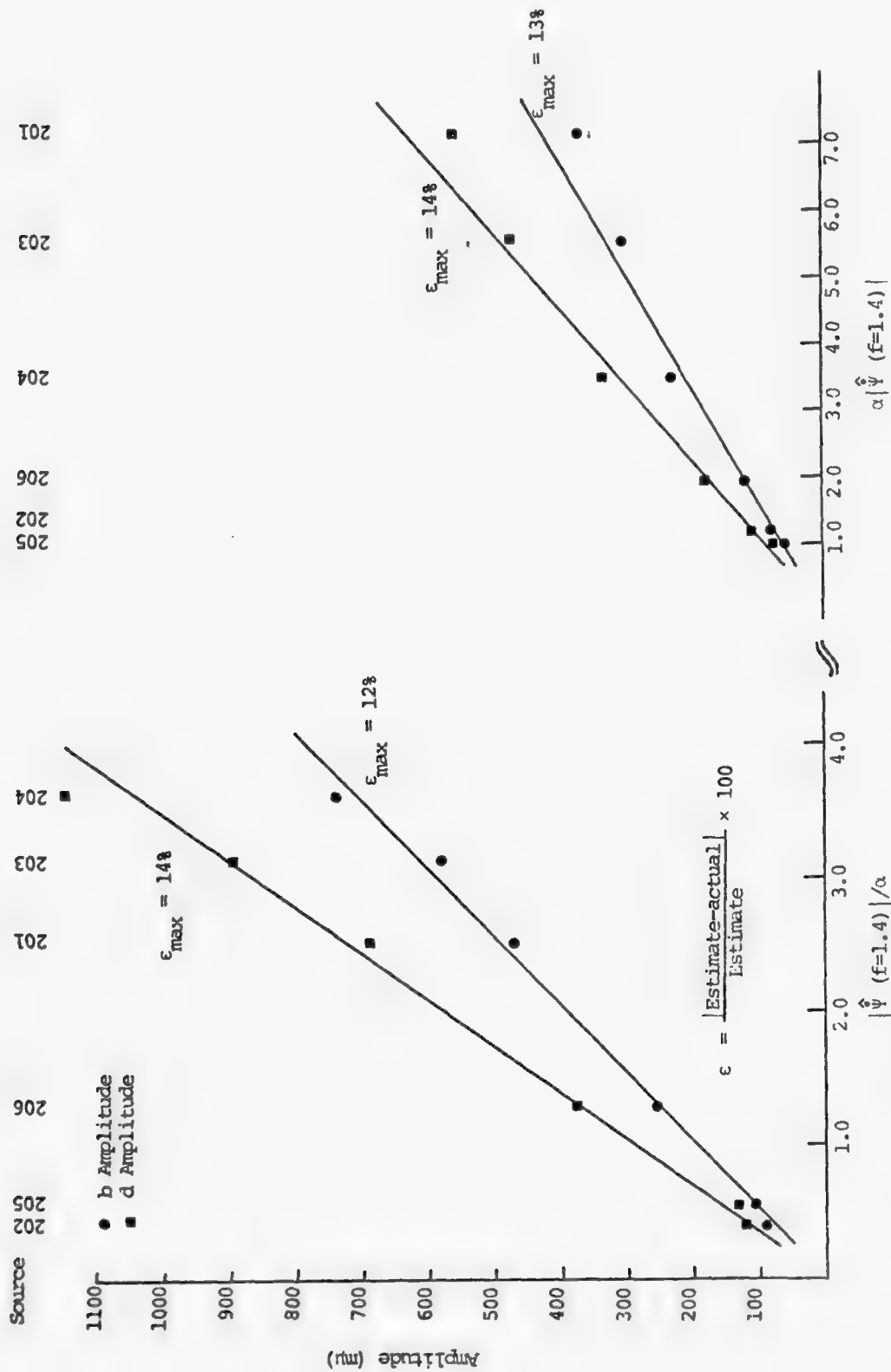
near 1.4 Hz. The accuracy of the scaling relationship discussed above can then be assessed by plotting the b and d amplitudes versus  $|\hat{\Psi}(f=1.4)|/\alpha$  for case 1, where the source region is homogeneous and versus  $\alpha|\hat{\Psi}(f=1.4)|$  for case 2 where a layered geology is introduced below the source. The plots are shown in Figure 3.2.

The average ratio of abscissa to ordinate was computed for each of the data sets of Figure 3.2 and a line representing the average slope appears on the plot. An estimate of the deviation from this line was made and the maximum deviation ( $\epsilon_{\max}$ ) is also indicated on the plot.

Figure 3.2a shows that the scaling of source displacement spectral amplitudes with  $\hat{\Psi}(\omega)/\alpha$  provides an excellent approximation to the scaling of the time domain amplitudes from the synthetic seismograms of Figure 2.1. When layering is introduced, we see in Figure 3.2b that the spectral scaling with  $\alpha|\hat{\Psi}(\omega)|$  provides just as good an approximation. In summary, Figure 3.2b provides assurance that we understand how the direct P wave scales with the source spectrum and elastic properties of the source material. Further, Figure 3.2a shows the kinds of errors that are inherent in the procedure, even when we know exactly how each frequency component of the seismogram scales.

The next complication to be introduced is the free surface effect. Inclusion of the free surface in our calculations actually has two effects. Most important is the addition of the large negative phase, pP, to the seismogram. Also, the energy reflected by the impedance contrast between the source and basement materials then reflects back from the free surface and can influence the seismogram's character. The importance of this latter effect depends, of course, on the severity of the impedance mismatch and on its depth. In general, though, the effect is rather small.





a. Homogeneous source crust  
b. Layered source crust

Figure 3.2. Agreement of measured synthetic seismogram amplitudes with theoretical scaling relations. No free surface reflection is included in the calculation.

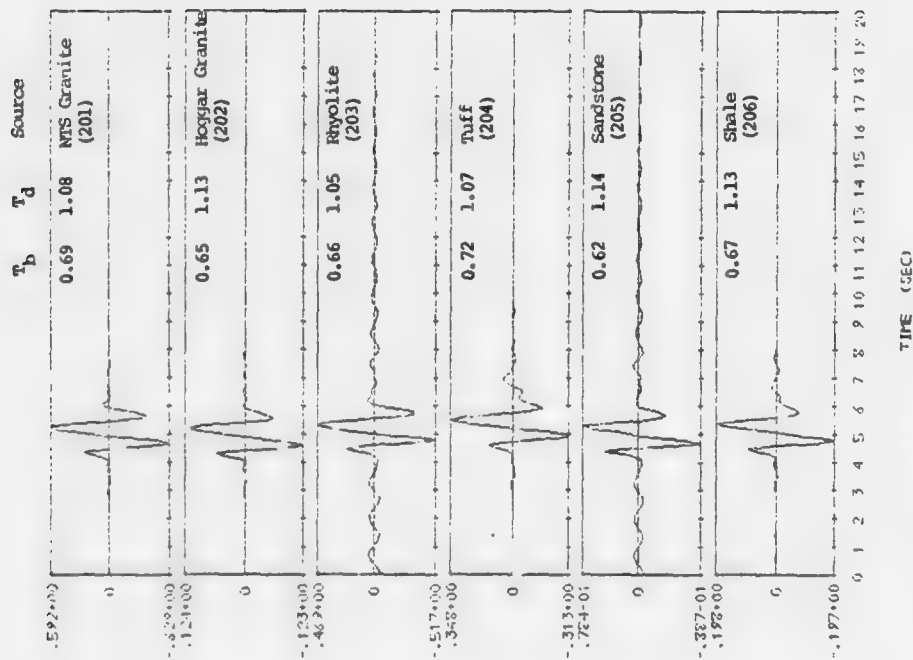
The seismograms for cases 3 and 4, where the free surface is included in the calculation, are shown in Figure 3.3. For computing these seismograms the crustal structures of Table 3 were used. First, in Figure 3.3a we take the delay time between P and pP (the P-pP lag) to be constant at 0.6 seconds. Second, in Figure 3.3b we consider the depth to be fixed, thus the P-pP lag varies with  $\alpha$ . Since the source material is assumed to extend to the free surface (Table 3),

$$P - pP \text{ lag} = \frac{2H}{\alpha} \cos \theta, \quad (3.6)$$

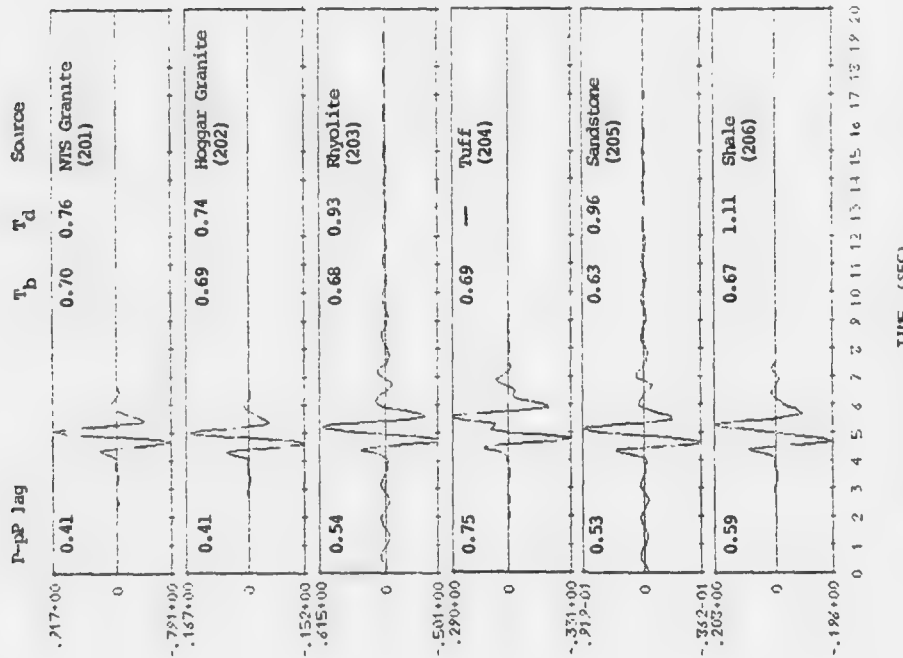
where H is source depth and  $\theta = \sin^{-1} \alpha/c$ , where  $c = 12.69$  km/sec for these calculations. We should point out that to obtain the desired values of 0.6 seconds for the lag, some of the crustal structures of Table 3 were modified by increasing the thickness of the first layer while leaving the rest of the structure unchanged.

Measurements of the amplitude and period of the b and d phase were made for the seismograms of Figure 3.3, with the exception that no consistent d phase could be measured on the Source 204 record of Figure 3.3b. We saw in Figure 3.2 that the scaling of the direct P wave is quite accurately represented by  $\alpha |\hat{\Psi}(f_p)|$  where  $f_p$  is the dominant frequency in the transient signal. Let us then see how much this scaling is compromised by the addition of the free surface effect, especially pP. We note that the composite pulse making up the d phase has a period quite different than the 0.7 second periods that we know dominate the P and pP phases taken separately.

The b and d amplitudes are plotted versus  $\alpha |\hat{\Psi}(f=1.4)|$  in Figure 3.4. The plot format, procedure for fitting the line and determining  $\epsilon_{\max}$  are as in Figure 3.2. First, consider Figure 3.4a, the case where the p-pP lag is constant.



a. P-pp lag = 0.6 seconds



b. Depth held fixed; P-pp lag is as indicated

Figure 3.3. Synthetic seismograms for cases 3 and 4 described in the text. The ripple appearing on some of the records is due to error in the numerical Fourier transform.

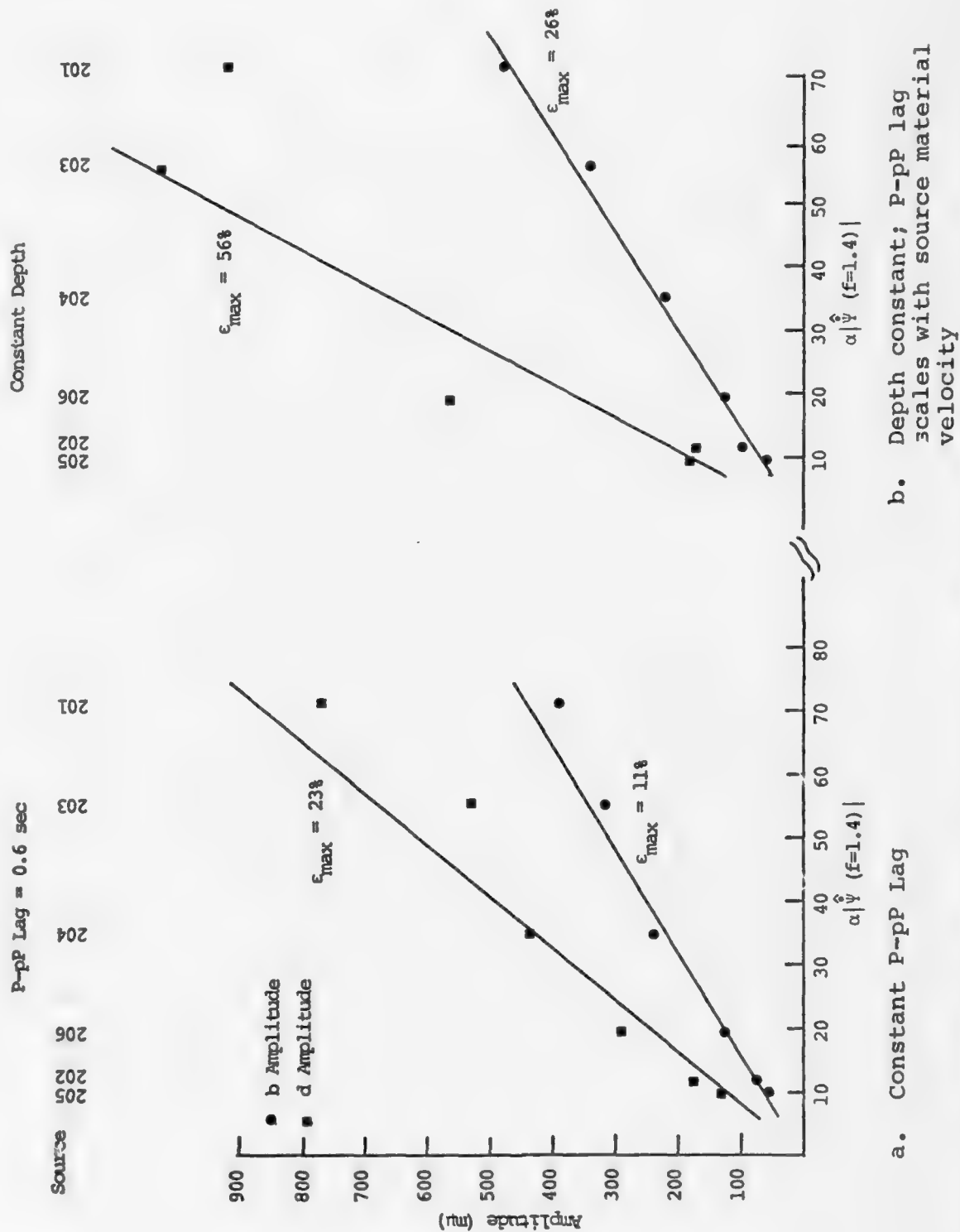


Figure 3.4. Agreement of measured synthetic seismogram amplitudes with theoretical scaling relations. The free surface effect is included.

We note that the agreement of the b phase data with the scaling relation is about as good as in Figure 3.2. For the 0.6 second lag time the pP phase has a small and consistent effect on the b phase. The agreement begins to deteriorate for the d amplitude, but is still fairly good. This is an indication that the pP effect is consistent from event to event. We should mention that scaling with the source spectrum at a frequency closer to that of the d period, say  $f_p = 1.0$  Hz, gives worse agreement.

For the constant depth, variable lag time case, the data is plotted against  $\alpha|\hat{\Psi}(f=1.4)|$  in Figure 3.4b. Once again, for the b phase the agreement is reasonably good because the pP arrives too late to have a substantial effect. For the d phase, however, agreement with the scaling relation can be quite poor. For example, compare sources 201 and 203 or 202 and 205. Clearly, the pP phase has a major effect on the d amplitude.

In this section all features of the source-receiver travel path have been held fixed except for the crustal structure in the vicinity of the source. We saw that the scaling of seismogram amplitudes is given to quite good accuracy by  $\alpha|\hat{\Psi}(f_p)|$  except when this scaling is severely compromised by variations in the P-pP lag time. In principle we should be able to correct for this latter effect and this is the subject of the next section.

#### SUMMARY

1. Given the equivalent source, then teleseismic ground motion is directly proportional to  $\alpha$ . The single most important near source material property is  $\alpha$ . We should insist that this parameter be measured in situ.
2. If possible, use the b amplitude to obtain magnitude. For the yields and DOB of interest, this amplitude is not significantly contaminated by pP.

#### IV. BODY WAVE AMPLITUDE CORRECTION FOR pP

In the previous section we saw that the free surface reflected phase, pP, has a significant effect on measured body wave amplitudes. This effect is investigated systematically in this section. We compute a series of theoretical seismograms for which all parameters are fixed except the depth of burial or P-pP lag. The source is chosen to be that which was computed specifically for the Pahute Mesa rhyolite event MAST (Figures 2.1 and 2.2). The source region crustal model is given in Table 4.

The synthetic seismogram computations were carried out in a similar fashion to those of the previous section. However, a more complex procedure was used for specifying the upper mantle and receiver crust transfer functions,  $T_M(\omega)$  and  $T_R(\omega)$ . A more detailed description of this procedure has been given in previous  $S^3$  reports (e.g., Bache, et al., 1975; Barker, et al., 1976; Bache, et al., 1976). Haskell matrix methods (Haskell, 1962) are used for computing  $T_R(\omega)$ . However, the receiver structure was taken to be an average continental crust which has almost no effect on frequency content of the seismogram. For the upper mantle elastic response a generalized ray theory program is used (Wiggins and Helmberger, 1974). The upper mantle model was a slightly modified version of C2 given by Anderson and Hart (1976) and the epicentral distance was 3730 km. At this range the upper mantle response is nearly independent of frequency and the approximation (3.3) is not bad. The instrument response was taken to be the LRSM short period nominal response for all the computations.

Seismograms were computed at depths ranging from 0.3 to 3.0 km. The P-pP lag times then varied between 0.13 and 1.31 seconds. The suite of seismograms was computed for three cases with differing dominant frequencies. These are:

TABLE 4  
SOURCE CRUSTAL MODEL FOR DEPTH OF BURIAL STUDY

<u>Depth (km)</u>	<u>Thickness (km)</u>	<u><math>\alpha</math> (km/sec)</u>	<u><math>\beta</math> (km/sec)</u>	<u><math>\rho</math> (gm/cm<sup>3</sup>)</u>
3.1	3.1	4.3	2.4	2.6
7.0	3.9	4.7	2.6	2.6
13.0	6.0	5.4	2.7	2.7
20.0	7.0	6.0	3.5	2.8



1. Yield = 300 kt;  $T/Q = 1.05$ ,
2. Yield = 300 kt;  $T/Q = 0.7$ ,
3. Yield = 10 kt;  $T/Q = 1.05$ .

Other than the yield and  $T/Q$ , the parameters for the three sets of seismograms are identical in all respects.

The synthetic seismograms for the three cases listed above are shown in Figures 4.1 through 4.3. The P-pP lag is indicated on each record. To provide a standard of comparison we also computed the direct P wave seismogram for each case and this is shown at the top of each figure. The direct P wave computation was done by taking the first layer of the crustal structure of Table 4 to be a halfspace rather than having a free surface.

Standard measurements of the b and d phases were made. The cycle for the d phase measurement is indicated on each record by a bar at the zero crossing. Since these are theoretical seismograms given in digital form, the peak-to-peak amplitude and time (half the apparent period of the cycle) can be measured with extraordinary accuracy. In fact, measurements are generally done automatically using parabolic fits at each peak rather than by hand. As the P-pP lag time increases, phasing becomes apparent in the maximum cycle. For some of these seismograms we continued to use the peak-to-peak amplitude but took the half period from a zero-to-zero measurement on the uncontaminated portion of the wavelet. The seismograms where this was done are indicated by an H symbol above the measured half period. A consistent determination of this period is quite important because of the instrument correction.

The measured periods of the b and d phases,  $T_b$  and  $T_d$ , are given on each seismogram. We see that the period of the b phase increases steadily until the lag is about 0.53 -

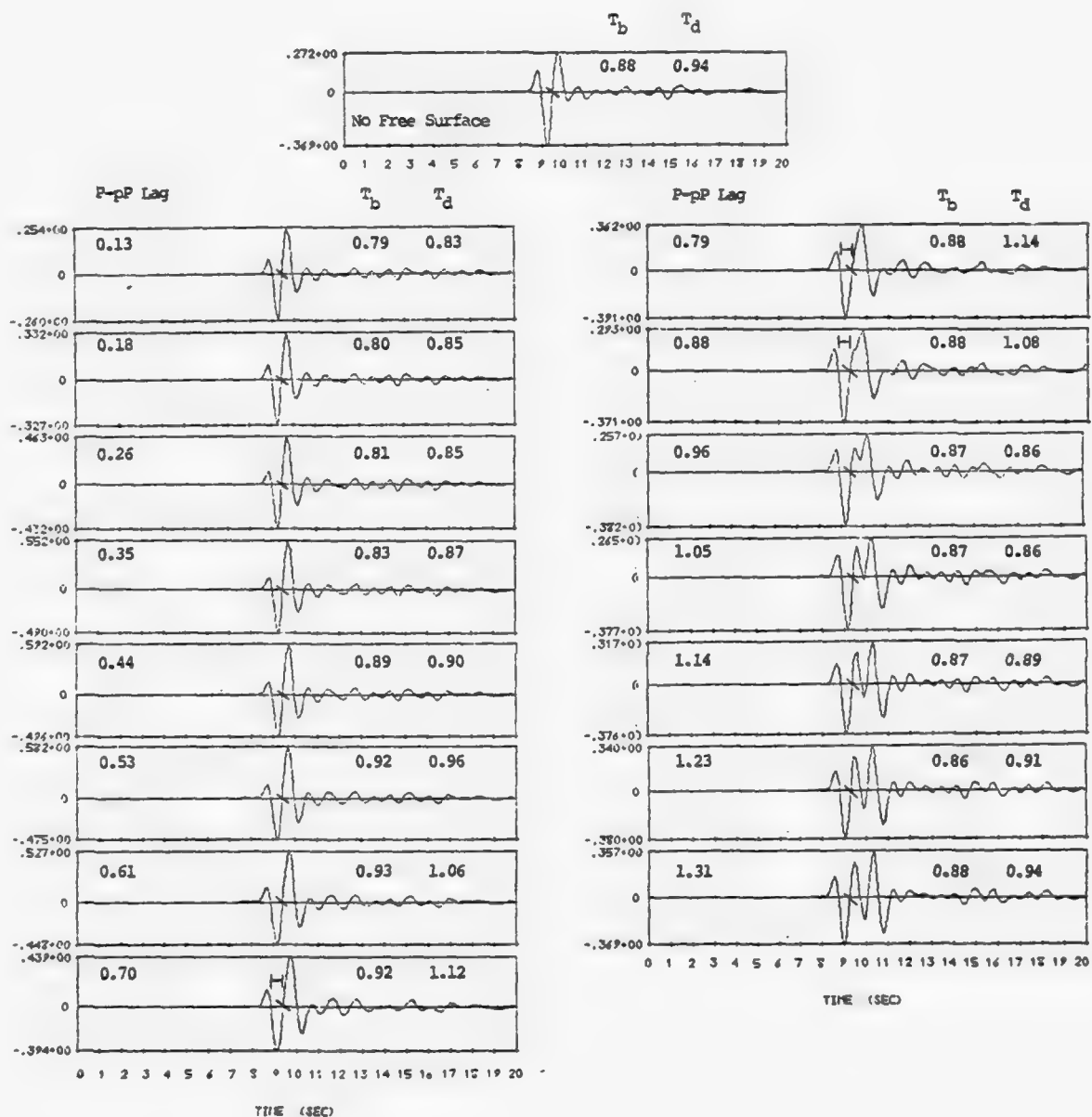


Figure 4.1. The effect of changing P-pP lag time on an explosion in rhyolite at Pahute Mesa, NTS. The yield is 300 kt and  $T/Q = 1.056$ .

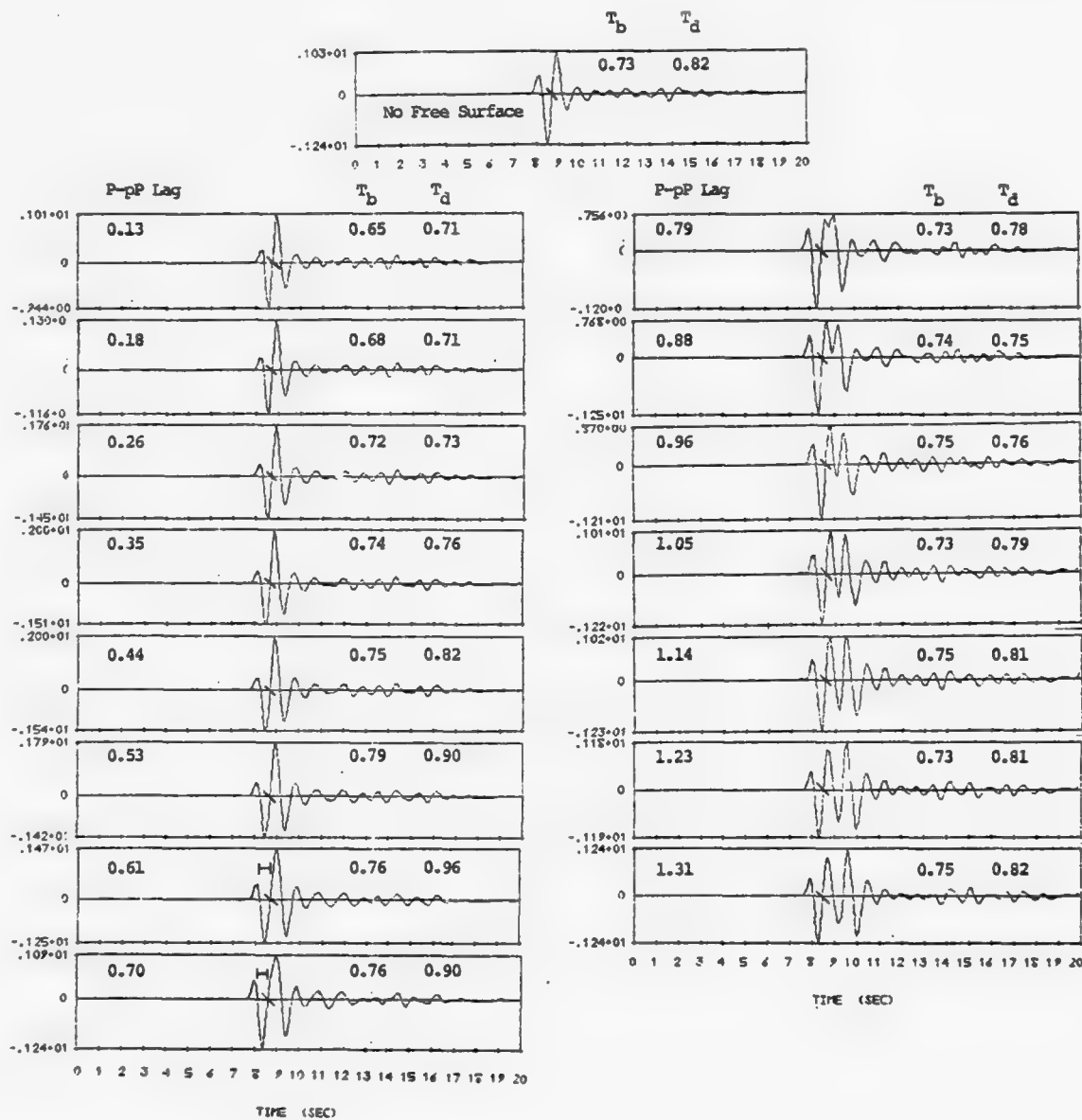


Figure 4.2. Seismograms identical to those of Figure 4.1 except  $T/Q = 0.7$ . The yield is 300 kt.

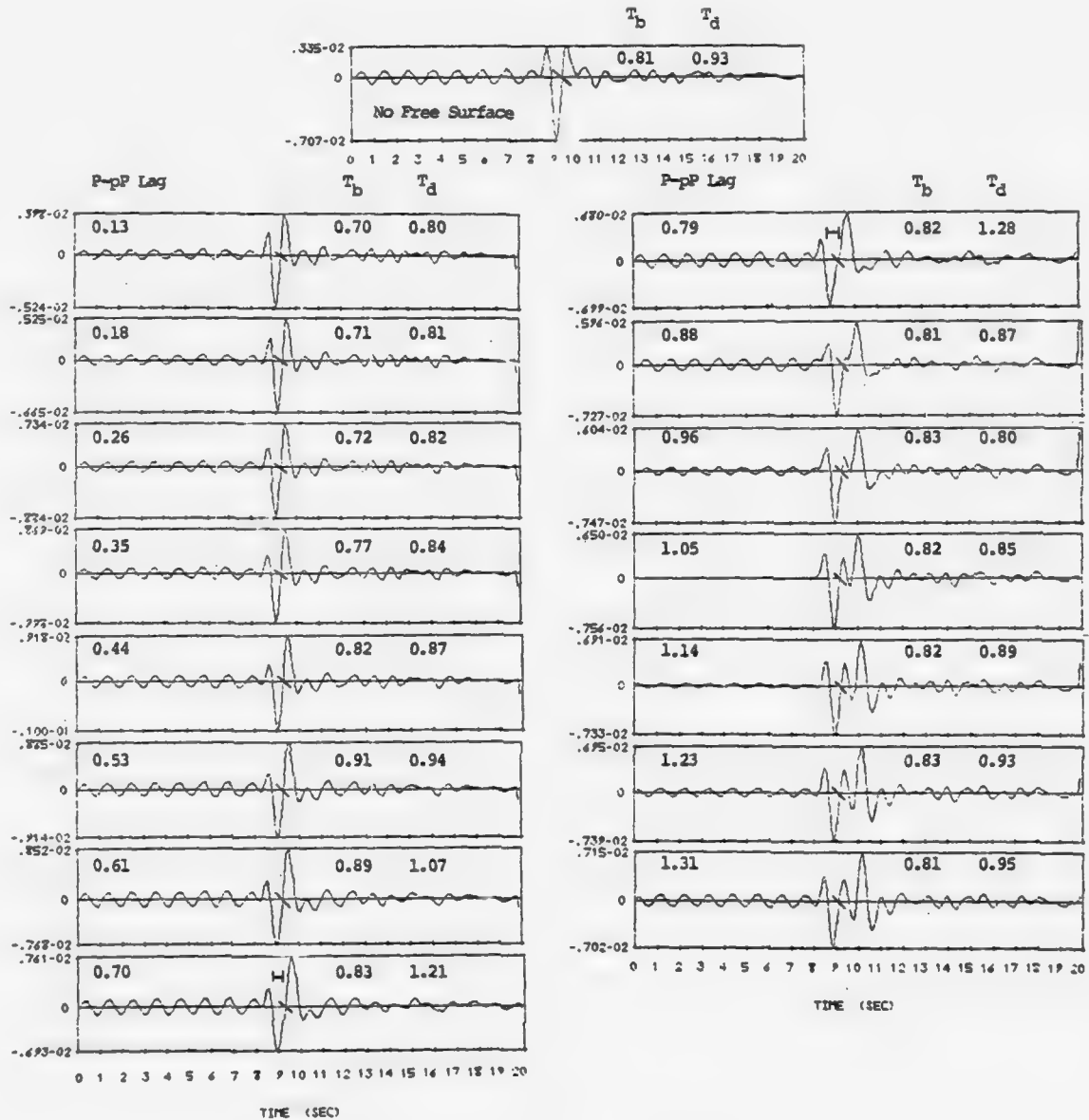


Figure 4.3. Seismograms identical to Figure 4.1 except the yield is 10 kt. The T/Q is 1.056. The ringing is due to the numerical difficulties with the Fourier transform. It seems to have minor effect on the results.

0.61 seconds, then decreases a bit to its final level. The d phase period behaves more erratically as the P and pP phases pull apart and we change the quantity being measured. Still these measurements are probably the most consistent and accurate possible. We also point out that at the greatest lag time the P and pP phases are essentially separated as can be seen by comparing to the direct P wave seismogram at the top of each figure.

Our objective is to construct curves showing how pP changes the teleseismic amplitudes from the values for the direct P wave taken alone. As we saw in Section III, it is the direct P wave that is most indicative of yield if we know the properties of the emplacement material. Therefore, we normalize the b and d amplitudes from the seismograms of Figures 4.1 - 4.3 to the values for the direct P wave taken separately. The results are plotted versus P-pP lag time in Figures 4.4 and 4.5.

For the b phase corrections, Figure 4.4, we see that the behavior is not markedly different for the three cases studied. At very short lag times the b phase amplitude is reduced by factors ranging down to 0.6 and below. We should point out that lag times less than, say, 0.4 seconds are extremely unlikely for the large explosions of interest. For the 300 kt explosion the b phase normalized amplitude peaks at around 1.2 so the amplitude is not significantly enhanced for any lag time. The peaking for the 10 kt event is somewhat higher but the noisy character of the records makes the results a bit suspect. In summary, we conclude that for likely values of the P-pP lag, the b phase is closely representative of the direct P wave.

The d phase correction curves, Figure 4.5, are quite interesting because the correction can be significant. First we note that except for lag times in the 0.6-0.9 second range the curves are pretty much the same for all three cases.

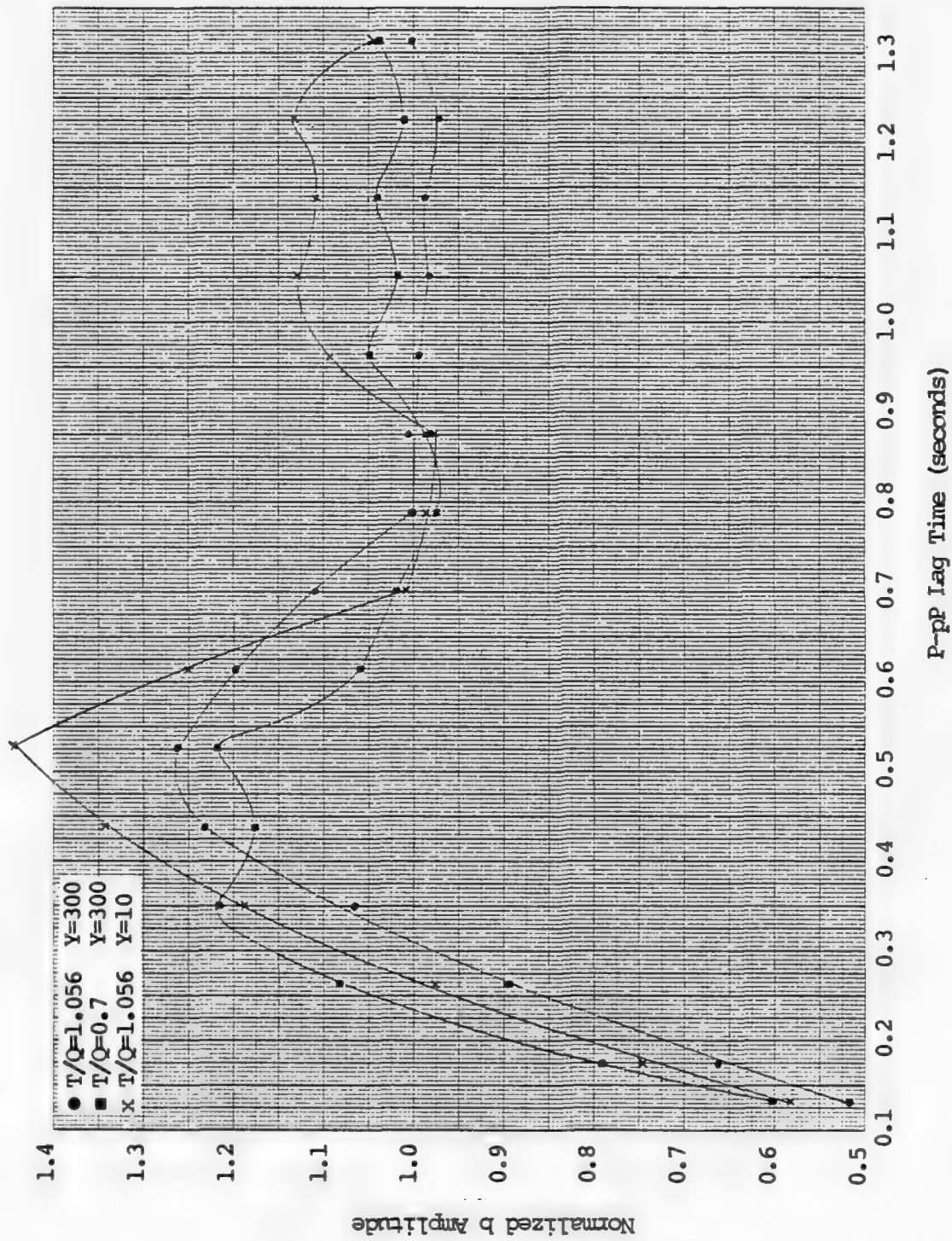


Figure 4.4. Corrections to the b amplitude for P-pP lag time.

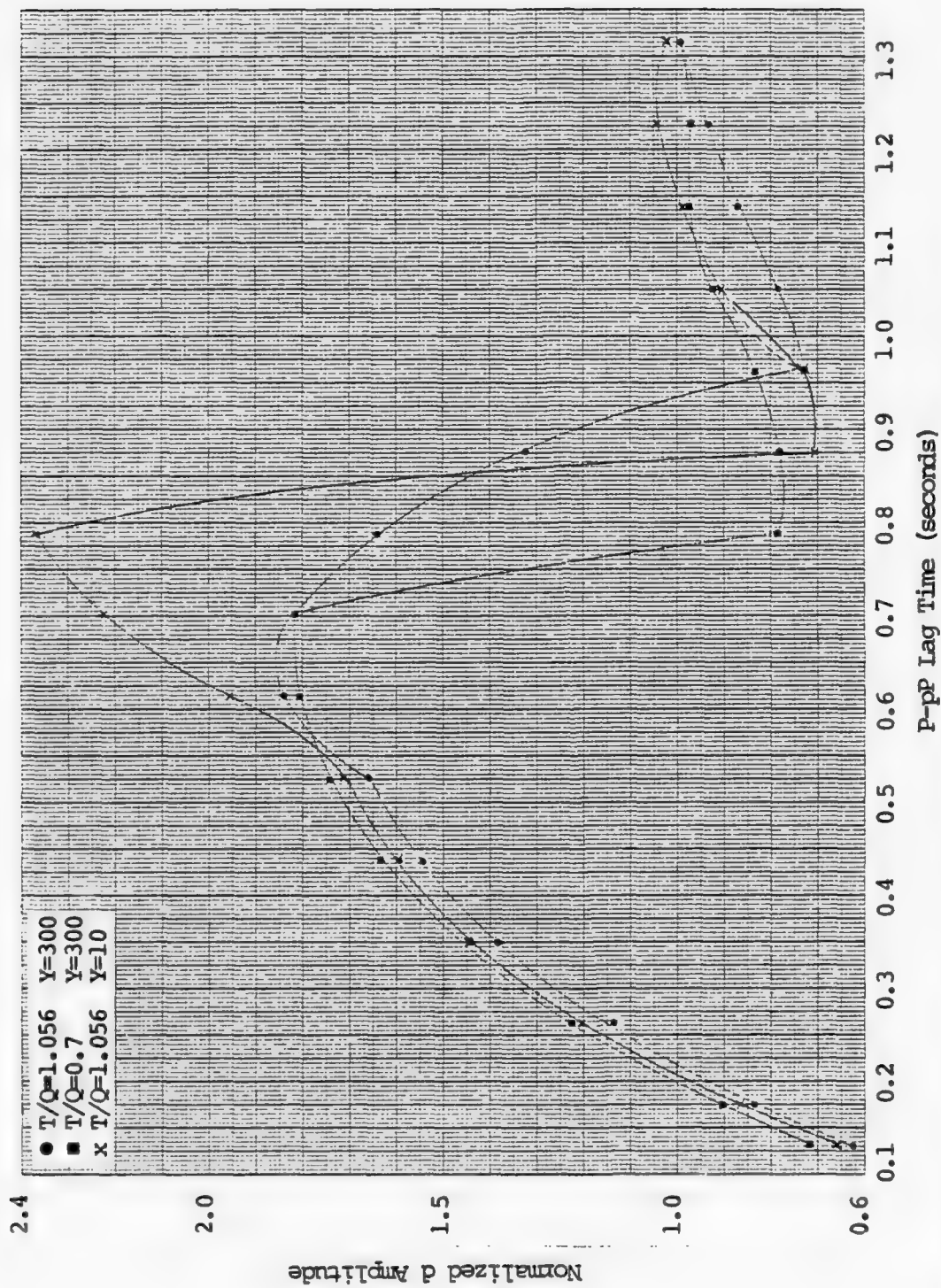


Figure 4.5. Corrections to the maximum (d) amplitude for P-pP lag time.



In this lag time range the P and pP phases separate and the apparent period measurement cannot be made consistently. The character of the normalized amplitude curves, especially the sharp discontinuities, is probably more due to rapid changes in the instrument correction factor than to changes in the amplitude of the actual ground motion. Still, we are following conventional procedure.

The peak of the d amplitude correction curve occurs at about 0.6-0.7 seconds for the 300 kt events. At the peak the amplitude is more than 1.8 times as large as that from the direct P wave itself. More important, the correction curve falls away rapidly on either side of the peak so events with lags near these values can appear considerably larger than those with lags a few tenths of a second different.

For the 10 kt event the d amplitude correction curve peaks at an extraordinarily high value, nearly 2.4. The high value is due to the long apparent period of the d phase and commensurate instrument correction factor. Is this an aberration? Perhaps not. The only different between cases 1 and 3 is that the source spectrum is shifted to higher frequencies by a factor of 3.1.

In the following section the practical consequences of the depth correction factors presented here will be explored by applying them to actual data.

#### SUMMARY

If the d amplitude is used to obtain  $m_b$ , then both the pP interval time and the instrument response characteristics must be available before this measurement can be used to obtain the amplitude of the direct P wave.

## V. MAGNITUDE-YIELD SCALING INCLUDING CORRECTIONS FOR DEPTH OF BURIAL

In this section we apply the theoretical P-pP lag time corrections developed in Section IV to a small set of actual data. The results are therefore quite preliminary, but intriguing.

The data is that compiled by Alewine, et al. (1976) for a group of Pahute Mesa events. This data is presented in the form of magnitude ( $m_b$ ) estimates based on the maximum amplitude ( $d$  phase) within the first three cycles of the P wavetrain recorded at teleseismic distances. The magnitude estimates were determined from measurements at a number of stations, carefully averaged to remove sources of error or bias. From the data set we select a number of large yield events detonated below the water table at Pahute Mesa, NTS. Thus, it would seem that the normalized  $d$  amplitude curve for 300 kt,  $T/Q = 1.05$  from Figure 4.5 is quite appropriate and will be used to correct the observed  $m_b$  values.

In order to apply the corrections, estimates of the P-pP lag times are required for the events under consideration. Several sources were used to estimate this quantity.

First, we need delay times from published reports by Kulhánek (1971) and Cohen (1975). These authors employed the spectral null technique in order to determine P-pP delay times for several Pahute Mesa events. Using these delay times and the amplitude correction curve of Figure 4.5, the magnitude estimates from Alewine, et al. were modified. The corrected  $m_b$  values are plotted versus explosion yield in Figure 5.1 as closed circles. The dashed open circles are the original (uncorrected) estimates from Alewine, et al.

Least squares fits were made to each set of data points in Figure 5.1. The results are as follows:

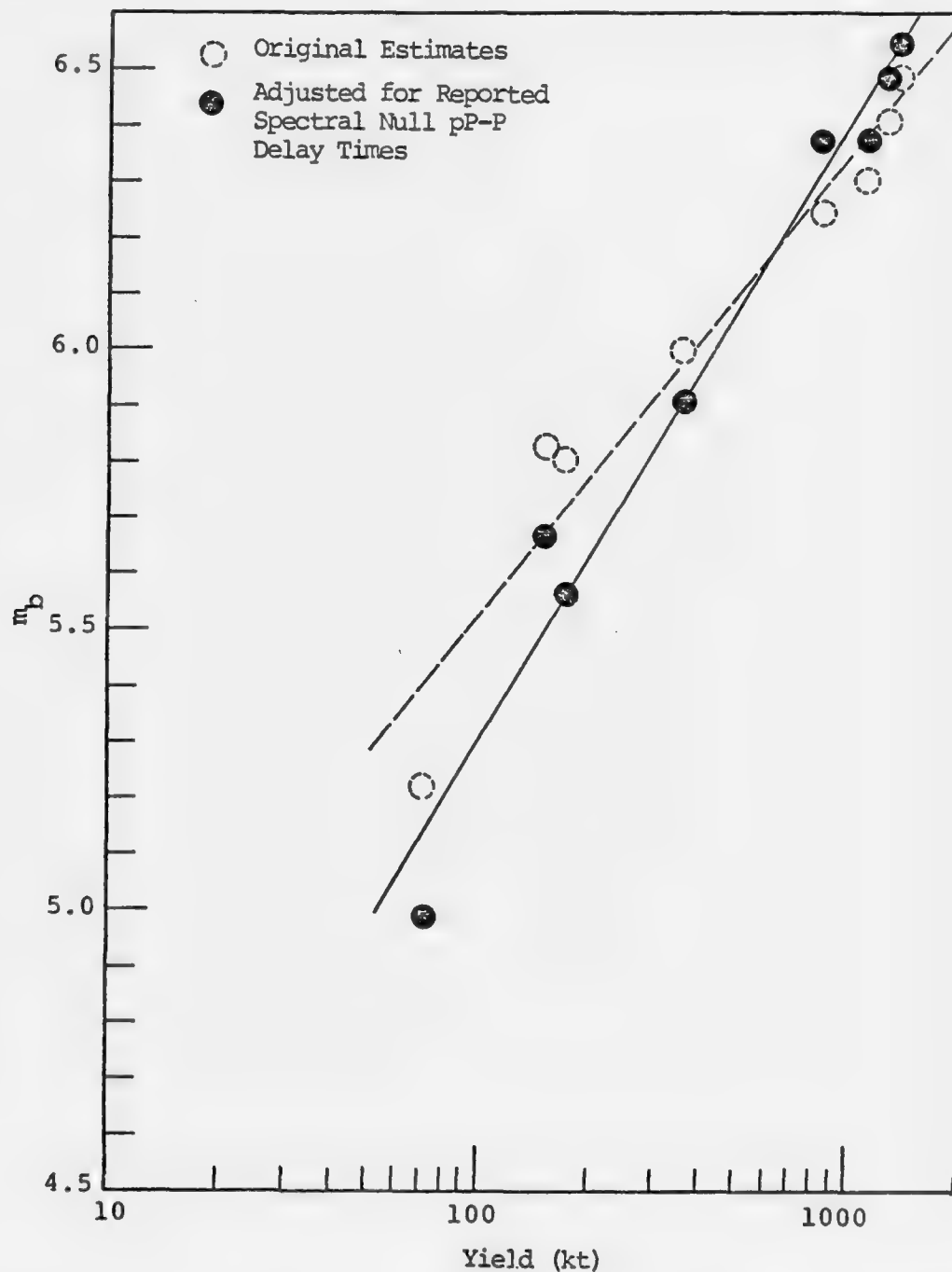


Figure 5.1. Original and revised (corrected) magnitude estimates versus yield for a population of Pahute Mesa explosions. The P-pP lag times for the corrections are based on spectral null and deconvolution techniques and are given by Kulhánek (1971), Cohen (1975) and Frasier (1972).

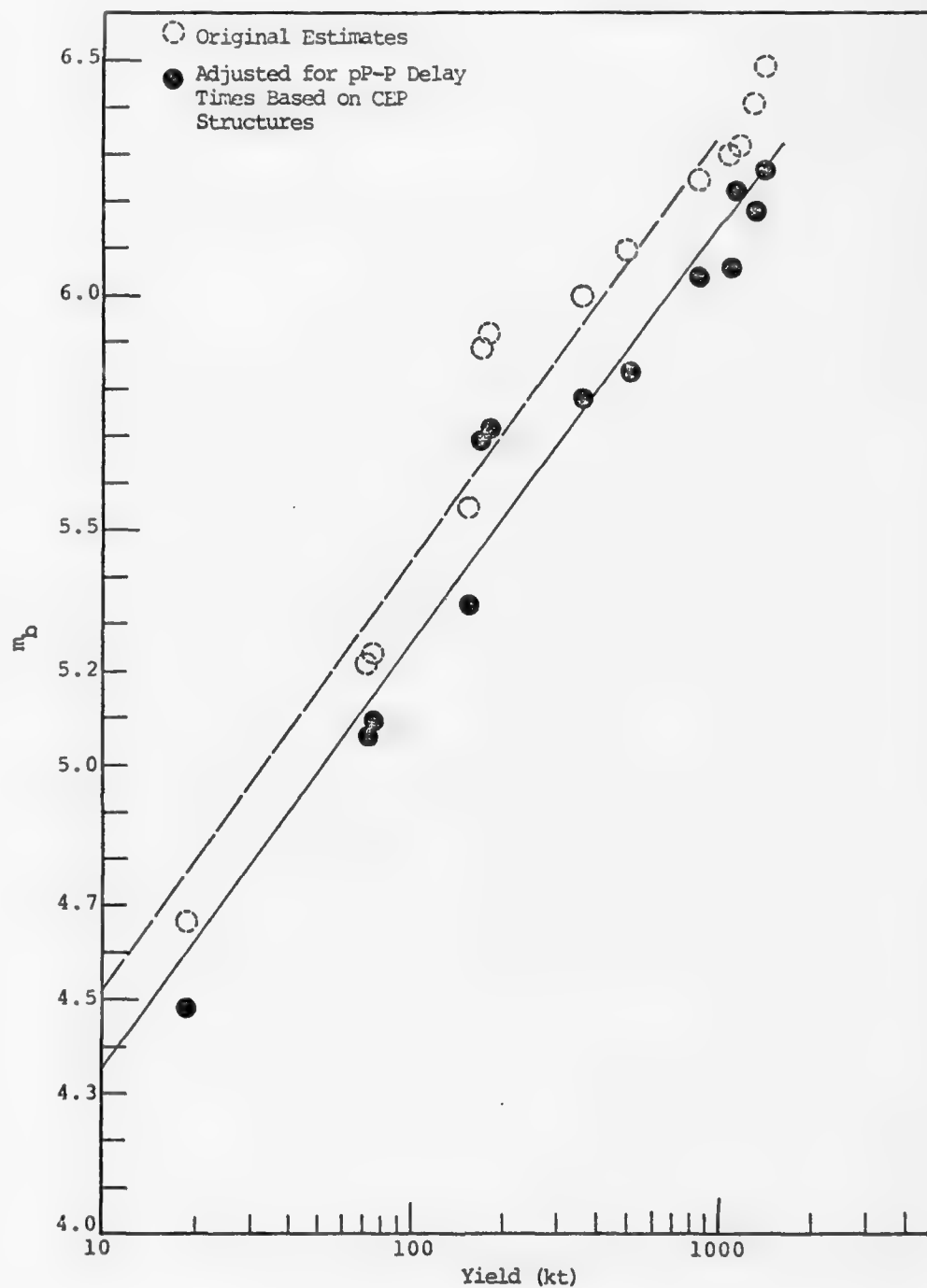


Figure 5.2. Original and revised (corrected) magnitude estimates versus yield for a population of Pahute Mesa explosions. The P-pP lag times for the corrections are based on the sonic velocities of the overburden material.

1. Adjusted  $m_b$ 's,  $m_b = 3.45 + 0.98 \log Y$ ,
2. Original  $m_b$ 's,  $m_b = 4.35 + 0.66 \log Y$ .

The most significant aspect of the data in Figure 5.1 is the fact that the slope of the straight line fit to the adjusted  $m_b$  values is quite close to unity (0.98), as compared to the much smaller slope for the original  $m_b$  estimates. Values of  $m_b - \log Y$  slopes between 0.75 and 0.95 are quite common in the literature for what we have here termed uncorrected  $m_b$  estimates. It seems that the pP effect is a strong contributing factor to this deviation from unit slope.

A second set of pP-P delay times was estimated for a larger (13 events) population of Pahute Mesa explosions. These delay times were based upon best estimates of the vertical two-way travel time between the explosion working point and the free surface. Detailed crustal structures from well log data were available for two of the explosions in this population. The remaining 11 explosions were detonated in the vicinity of one or the other of these two shots and the corresponding structures used to estimate travel times. In general, the delay times based on these crustal structures proved to be significantly shorter ( $\sim 0.2$  seconds) than those based on the spectral null techniques of Kulhánek (1971) and Cohen (1975) or the deconvolution procedure described by Frasier (1972). Using these estimates or delay times and the amplitude correction curve in Figure 4.5, magnitude estimates given by Alewine, *et al.* (1976) were adjusted and plotted versus yield in Figure 5.2.

The effect of the P-pP lag time correction on this population of events is significantly different from that in Figure 5.1. In this case, the corrections are all in the same direction and least square fits to original and corrected data give about the same results:

1. Adjusted  $m_b$ 's,  $m_b = 3.45 + 0.90 \log Y$ ,
2. Original  $m_b$ 's,  $m_b = 3.61 + 0.91 \log Y$ .

What is the meaning of the contradictory results of Figures 5.1 and 5.2? First consider the results of Figure 5.1 which were based on estimates of the P-pP lag time taken directly from recorded seismograms. While these may not be terribly accurate in any particular example, a number of authors have obtained about the same results. Further, these lag times are not far different from those inferred from direct measurements of the source-to-surface travel time when the explosion is detonated (Springer, 1974).

Refer to the normalized d amplitude correction curve of Figure 4.5. The reason for the change in slope that occurs in the data of Figure 5.1 when the P-pP lag correction is applied is quite simple. The larger yield explosions fall on the right side of the peak where the correction is small while the smaller yield explosions fall much nearer the peak on the left side where the correction is relatively larger.

Estimates of the P-pP lag based on the sonic velocity properties of the overburden rock are uniformly smaller than the estimates based on actual observations of the explosions. It's not entirely clear why this occurs, but it seems to be a fact. If we use the much lower sonic estimates of the P-pP lag, all the corrections to the data of Figure 5.2 fall on the left side of the peak in Figure 4.5. All the events are then corrected downward by a fairly uniform increment and the  $m_b$ -logY slope is not changed.

As we said at the beginning of the section, these results are preliminary, but quite intriguing. The corrections have been applied to only a few events in a single test region. The study should be broadened to include many more events in different test regions. Perhaps this will make a significant contribution to resolving some of the anomalies in the data.

### SUMMARY

What is the best way to obtain the pP interval time? If we use spectral nulls and/or deconvolve the recorded ground motion then we no longer have a predictive capability. Furthermore, this technique is subject to evasion possibilities.

We recommend that our shot data be used to determine the in situ P wave velocity measurements which best agree with the analysis of recorded teleseismic ground motion. If we find that we need the source-to-surface travel time for the calibration shots we should ask for it.

## VI. TWO "ANOMALOUS" EVENTS; FAULTLESS AND A FRENCH EXPLOSION AT THE HOGGAR TEST SITE

FAULTLESS is considered to be anomalous because it falls considerably above the empirical  $m_b$ -log Y curve based on events in similar source materials. Alewine, et al. (1976) give  $m_b = 6.51$  for FAULTLESS. Springer (1974) estimated the P-pP lag time for this event to be 0.8 seconds using the measured arrival time of the explosion shock wave at surface zero. Frasier (1972) gives 0.90 seconds and Kulhanek (1971) gives 1.02 seconds for the same quantity using teleseismic data. If we use Springer's value of 0.80 and the correction curve for  $Y = 300$ ,  $T/Q = 1.05$  from Figure 4.5, the revised magnitude estimate is 6.31, lower than the original estimate by 0.2 units.

If the revised magnitude for FAULTLESS is plotted in Figure 5.1, the anomalous magnitude-yield scaling for this event practically disappears. The revised magnitude plots within 0.1 magnitude unit of the least square fit (either  $m_b = 3.09 + 1.1 \log Y$  or  $m_b = 3.45 + 0.98 \log Y$ ) to the corrected magnitude data shown in Figure 5.1. Therefore, if we apply the P-pP lag correction in a consistent way to Faultless and a suite of Pahute Mesa events of similar yield and in similar emplacement materials, the FAULTLESS event no longer appears to be anomalous.

The French explosions at the Hoggar site in the Sahara are considered to be anomalous because they are essentially undistinguishable from United States granite explosions (e.g., PILEDRIVER) or an  $m_b$ -log Y plot. However, the French report that cavity radii in the Hoggar granite are 40 percent smaller than U.S. granite cavity radii, i.e., PILEDRIVER and HARDHAT. The source functions for events in NTS and Hoggar granite were presented in Section II. We



saw that the Hoggar source function is much smaller; the  $\alpha|\hat{\psi}(f_p)|$  is down by a factor of about 5 or 6 in the frequency range of interest. Further, we know that the NTS granite source gives a good match to both near field and teleseismic data for the PILEDRIIVER event (Bache, et al., 1975). How then can we explain the fact that the  $m_b$  is about the same for explosions of the same yield in the two granitic materials?

The first step to be taken is to see how much we really do underestimate the Hoggar body waves when all factors are taken into consideration. We have available a recording of a February 27, 1965, Hoggar explosion from the LRSM station HNME. We also have an estimate of the yield of this explosion. We then proceed to synthesize a seismogram at HNME using the Hoggar granite source (202), shown in Figure 2.1.

The factors we do not know are the crustal structure at the source (important only for the P-pP lag time), the upper mantle response and the best value of T/Q. We do not really know the crustal structure at the receiver or the instrument response either but we choose to use the same models as in our other work. The instrument response is taken to be the LRSM nominal. For the crust at the receiver we used the same transparent crust used in the synthetic seismogram calculations of Section IV. This is tabulated in Table 5. The elementary source crustal model used also appears in this table.

The upper mantle response is required at a distance ( $\approx 62^\circ$ ) outside our previous experience. We also wish to synthesize records at another LRSM station, RKON, which is even farther ( $\approx 77^\circ$ ). One of the best available upper mantle models is C2, recently published by Anderson and Hart (1976). The upper mantle response at the HNME and RKON distances was computed using our generalized ray theory programs and this model. We show in the next section

TABLE 5  
CRUSTAL STRUCTURES FOR SYNTHETIC SEISMOGRAMS FOR  
EXPLOSIONS AT THE HOGGAR TEST SITE

Source Structure

<u>Depth (km)</u>	<u><math>\alpha</math> (km/sec)</u>	<u><math>\beta</math> (km/sec)</u>	<u><math>\rho</math> (gm/cm<sup>3</sup>)</u>
2.40	5.33	3.78	2.67
5.20	5.80	3.45	2.67
21.20	6.00	3.50	2.80

Receiver Structure

2.58	3.67	2.31	2.40
4.84	5.42	3.27	2.60
11.61	5.80	3.45 .	2.60
20.00	6.00	3.50	2.80

that in this range the variation in amplitude from model to model is likely to be less than a factor of two.

Having disposed of all the "elastic" parameters, there are two "inelastic" parameters to be specified,  $T/Q$  and the P-pP lag time. The latter is classified as inelastic because we believe that inelastic effects are responsible for the lag time being considerably longer than that obtained from sonic velocities of the actual overburden material. These two quantities shape the seismogram and, to a considerable degree, determine its amplitude.

First, consider  $T/Q$ . It is widely believed that NTS is underlain by a region of anomalously low  $Q$ . Therefore, we would expect to require a Hoggar value of  $T/Q$  lower than the 0.95 - 1.05 values we have found appropriate for NTS events. The frequency content of the observed seismogram also strongly constrains  $T/Q$ .

For the P-pP lag time the only constraint is the shape of the recorded seismogram and, perhaps, past experience with events in similar materials. We synthesized seismograms for a number of lag time values and finally settled 0.80 seconds as giving the best match to the seismogram. This lag time is consistent with estimates for the lag time for PILEDRIVER made from teleseismic data. Since we don't know the burial depth of the Hoggar event, we can only conjecture regarding its depth relative to Piledriver.

Synthetic seismograms were computed at HNME for two values of  $T/Q$ ; 0.7 and 0.5. The two seismograms are shown in Figure 6.1 together with the observed record. The  $T/Q = 0.7$  seismogram matches the frequency content of the first few seconds of the observed record quite well. However, the amplitude is clearly too small. The  $T/Q = 0.5$  record is useful because it illustrates the fact that this quantity is narrowly constrained by the frequency content

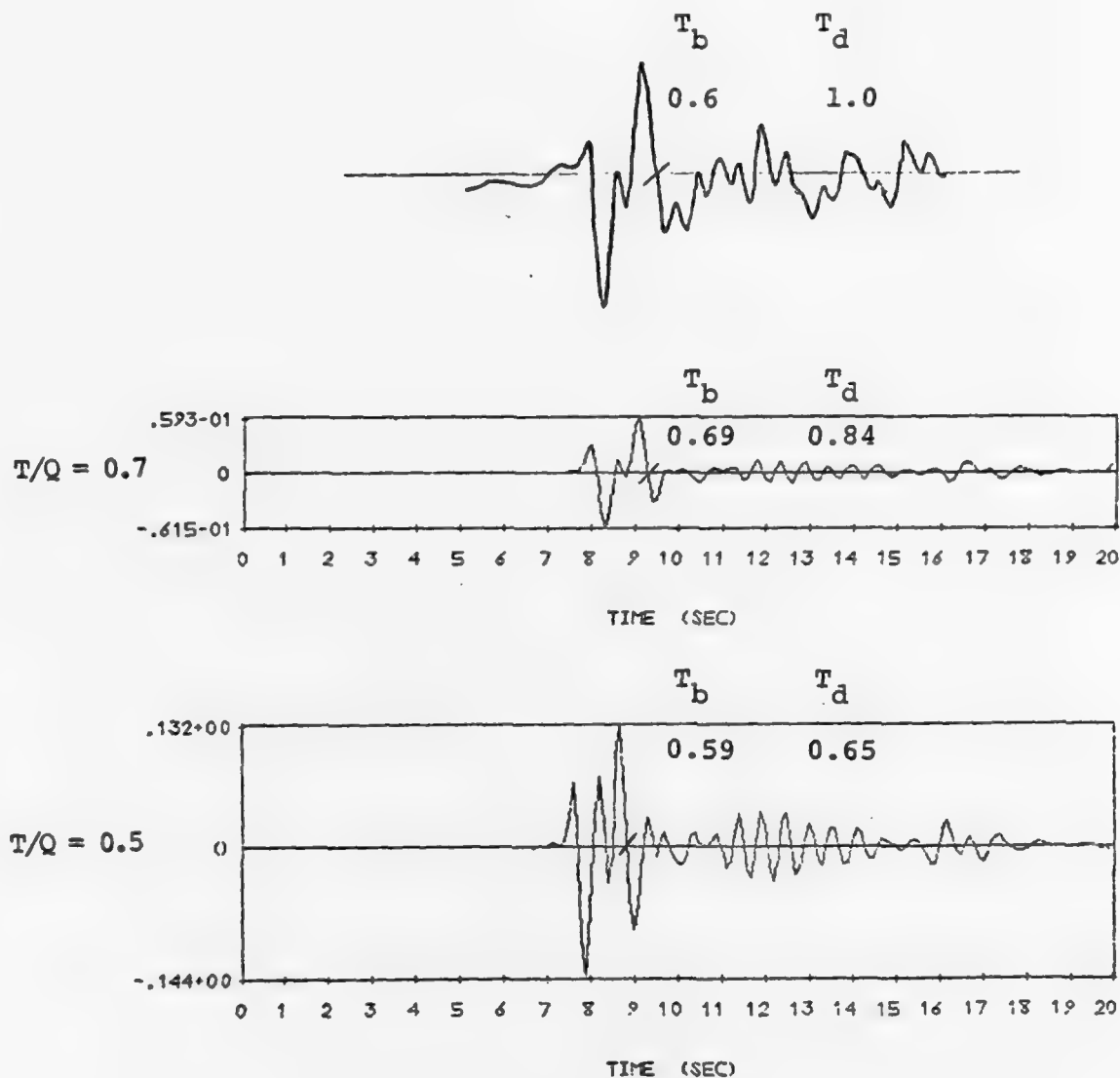


Figure 6.1. Comparison of synthetic (bottom two) and observed (top) short period vertical seismograms at HNME for the 27 February, 1965, Hoggar explosion. The time and amplitude scales are the same on all seismograms. The amplitude in microns at 1 Hz is indicated at the left on the synthetic records.

of the observations. Even though the amplitude of the  $T/Q = 0.5$  record more closely matches the observed amplitude, the dominant frequencies are clearly much too high. This fact cannot be changed by adjusting the P-pP lag time.

The synthetic seismogram with a P-pP lag time of 0.8 seconds and  $T/Q = 0.7$  gives an excellent match to the frequency content of the HNME observation. What can we say about the amplitude and, in particular,  $m_b$ ? There are two phases from which  $m_b$  can be measured on the observation. There are the b phase and the d phase which is indicated by a bar on the records of Figure 6.1. On the synthetic seismogram both the b and d phases give the same  $m_b$ , which is 5.57.

For the observed HNME seismogram we compute  $m_b = 5.78$  for the b phase and  $m_b = 5.93$  for the d phase. Based on empirical  $m_b$ -log Y plots on which this event appears, the average  $m_b$  seems to be about 5.70. We will therefore assume that most of the  $m_b$  peaks were from the b phase. With this assumption the HNME record is typical with  $m_b$  being a little less than 0.1 units above the average.

In summary, the theoretical  $m_b$  for HNME is about 0.2  $m_b$  units below the observed  $m_b$  for this station. The discrepancy is far less than the factor of five or six expected from comparison of the source functions. Further, the synthetic  $m_b$  is only 0.13 units lower than the average  $m_b$  for the Hoggar event. In short, our theoretical amplitudes match the observations to a factor of considerably less than two.

Seismograms appropriate for the RKON station were also computed with  $T/Q = 0.7$  and 0.5 and these are shown in Figure 6.2. For the  $T/Q = 0.7$  case, the theoretical  $m_b$  is 5.43 for RKON. This is somewhat lower than that of HNME but is still within 0.3  $m_b$  units (or a factor of two in amplitude) of the average for the event.

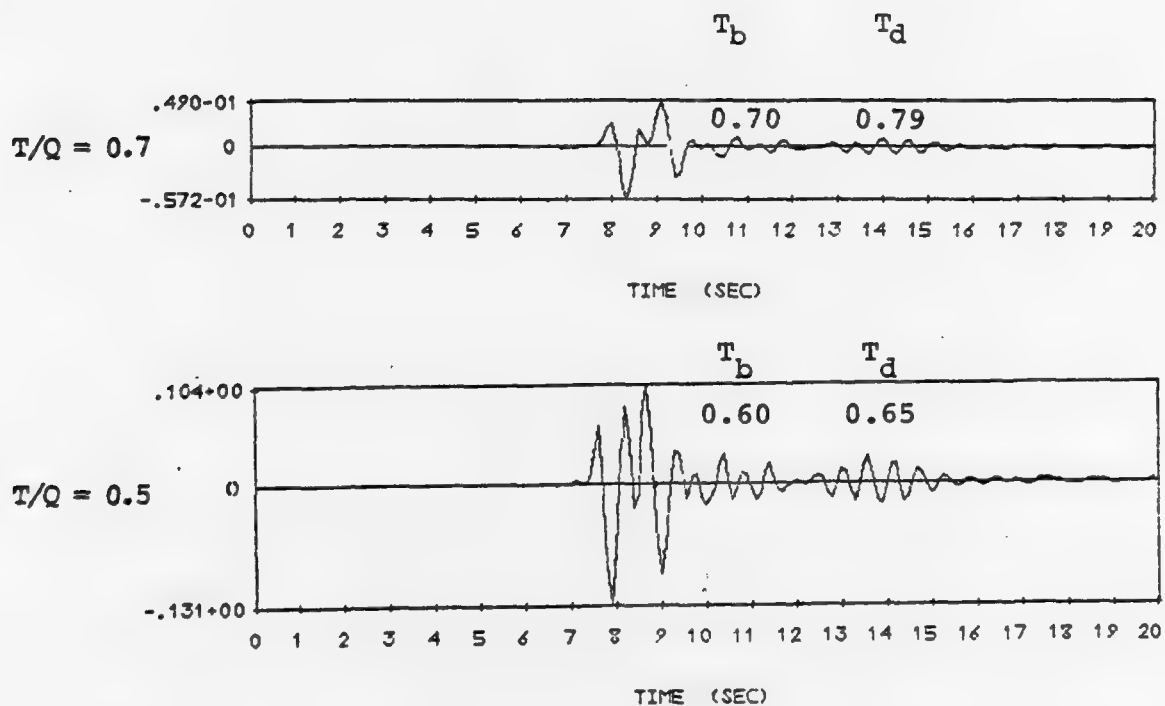


Figure 6.2. Synthetic short period vertical seismograms at station RKON for 27 February 1965 Hoggar explosion.

We synthesize the seismograms in Figures 6.1 and 6.2 to see how much we actually underestimate the Hoggar explosion body wave amplitudes. The answer is, not very much. As with FAULTLESS, we see that the Hoggar events are probably not anomalous to any serious degree.

#### SUMMARY

The FAULTLESS anomaly can be explained by a pP correction. The Hoggar "anomaly" can be explained by using a T/Q of 0.7.

## VII. EFFECT OF THE UPPER MANTLE ELASTIC PROPERTIES ON SHORT PERIOD SEISMOGRAMS

In this section we address the question, how much can the amplitude and waveform of teleseisms be influenced by reasonable changes in the upper mantle velocity profile? We restrict our attention to ranges between 20 and 36° and show the effect by computing synthetic seismograms with all factors held constant except the upper mantle velocity profile. The example chosen is the MAST explosion in rhyolite which was studied in some detail by Barker, et al. (1976).

The upper mantle models studied are perturbations of models HWNE (HelMBERger and Wiggins, 1971) and HWA (Wiggins and HelMBERger, 1973). The perturbations were not allowed outside the envelope of all possible models consistent with travel time, ray parameter and amplitude data for the western United States, as determined by Wiggins, et al. (1973). The changes from the starting models (which are fairly different from each other) were at most 0.3 km/sec.

The synthetic MAST seismograms were all computed with the MAST source (Figure 2.1),  $T/Q = 1.05$  and the instrument response was the LRSM nominal. Seismograms were computed for many models but only four examples which represent the extremes in their effect are discussed here. These models are denoted HWA-2, HWA-3B, HWA-6D and HWNE-3 and their velocity-depth profiles are shown in Figure 7.1.

Synthetic seismograms appropriate for the epicentral distance from NTS to the SDCS stations RKON, WH2YK and HNME are shown in Figures 7.2 through 7.4. These seismograms represent the extremes of the variation observed at these stations when perturbing the models under the constraints mentioned above. The signals at RKON and WH2YK are affected primarily by the structure 100 km above and below the 400 km



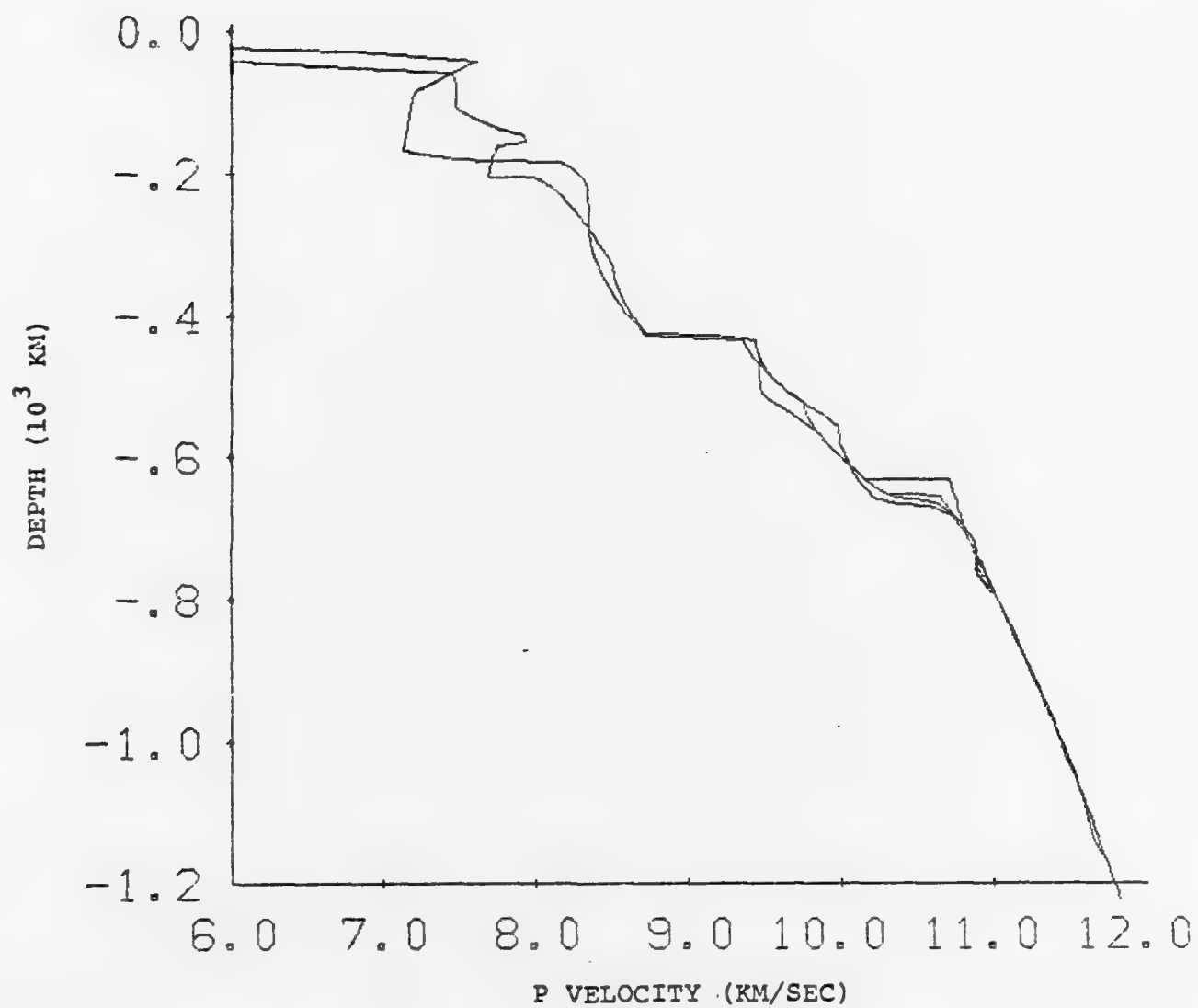


Figure 7.1. P wave velocity depth profiles for the four upper mantle models used to compute the seismograms of Figures 7.2 - 7.4.

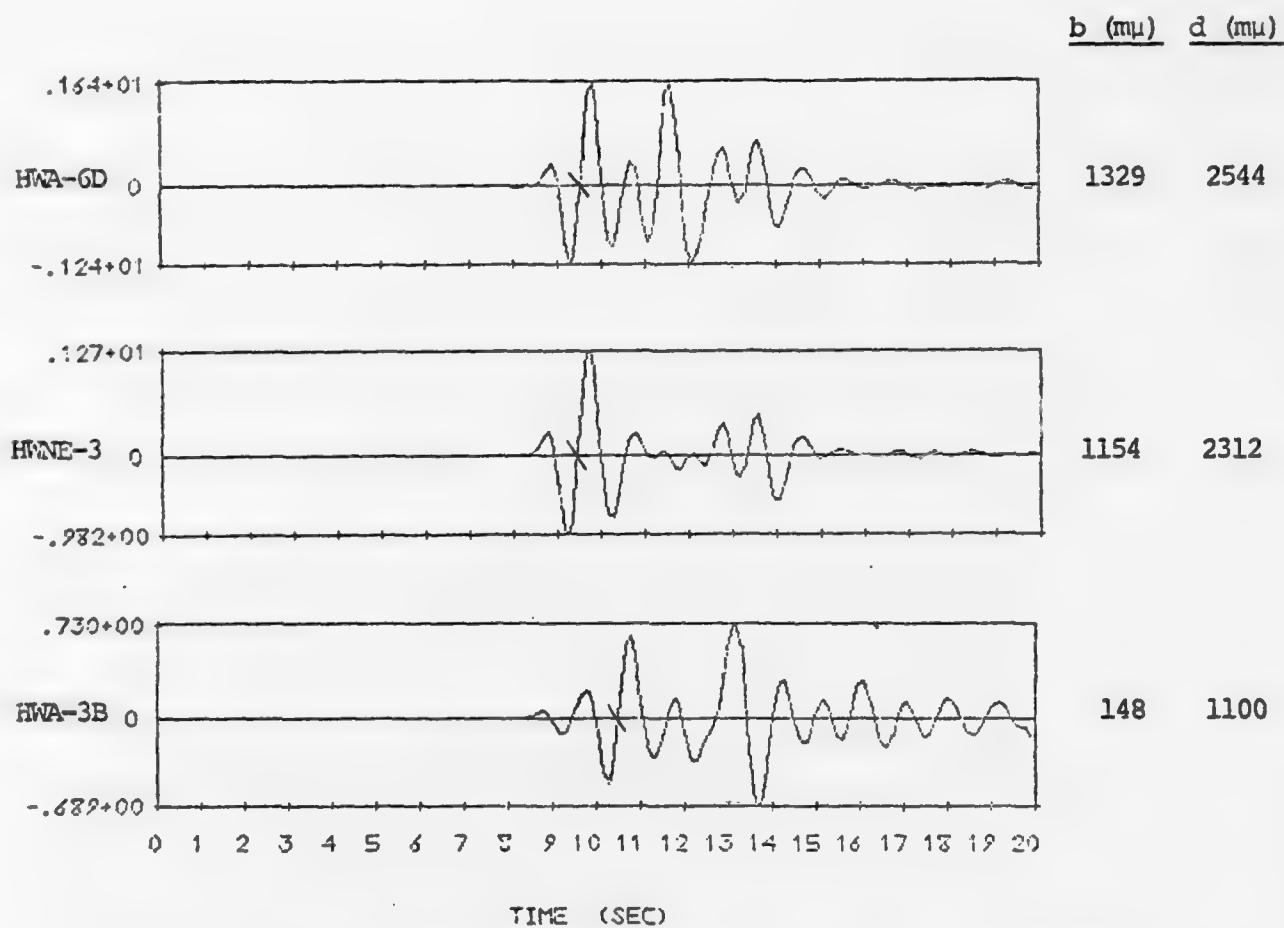


Figure 7.2. Variation in amplitude and waveform for three upper mantle models for MAST at station RKON.

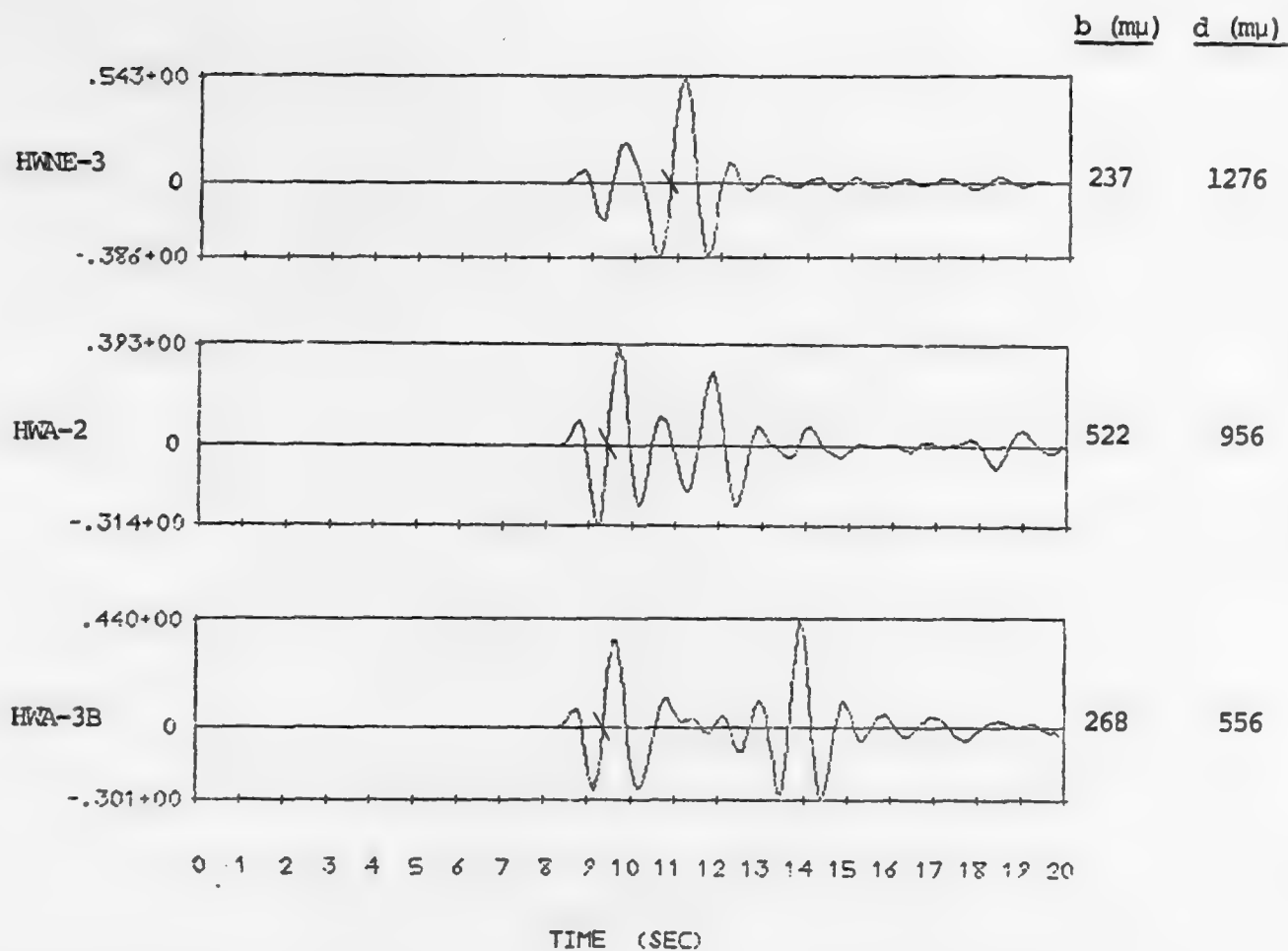


Figure 7.3. Variation in amplitude and waveform for three upper mantle models for MAST at station WH2YK.

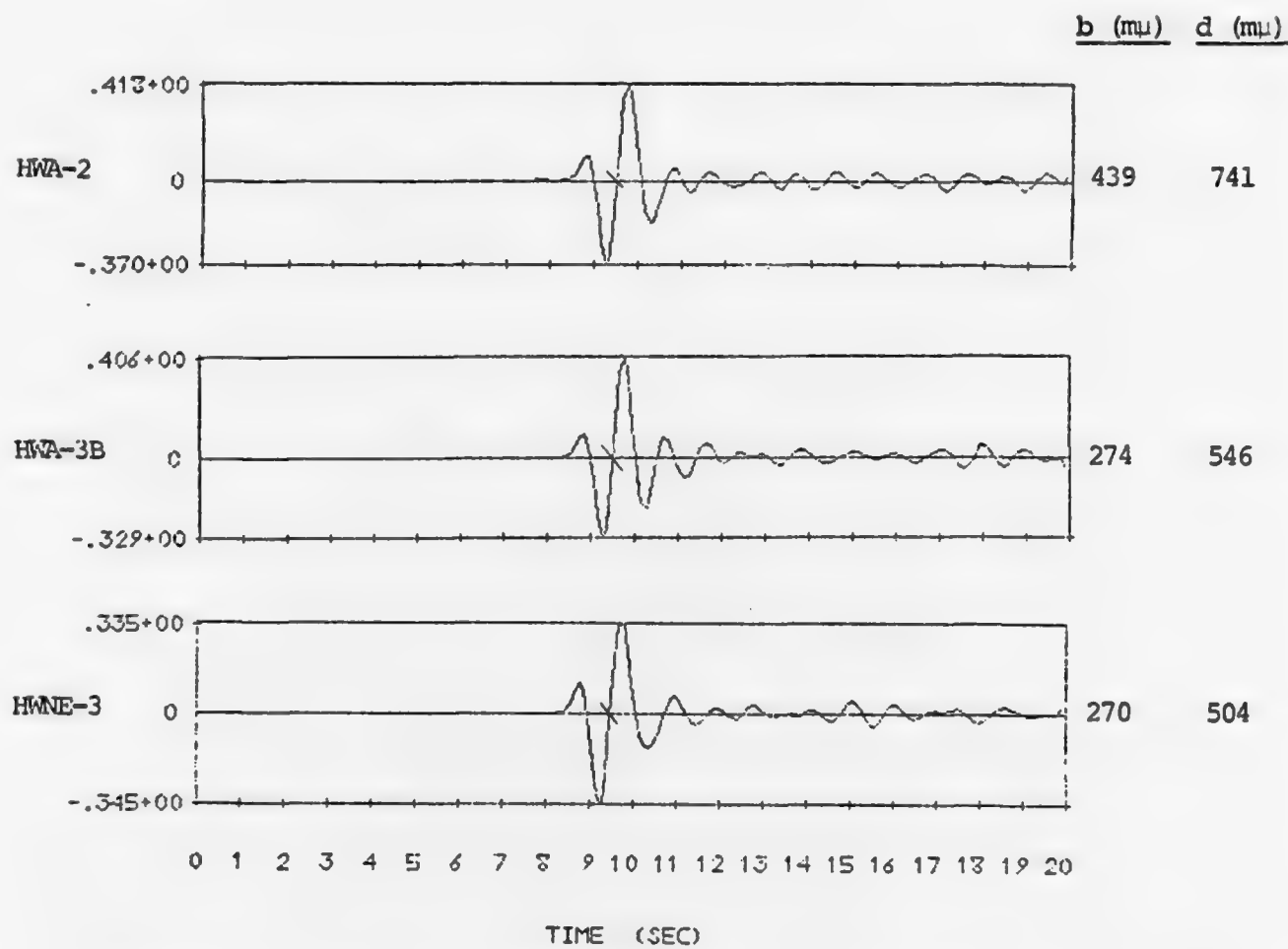


Figure 7.4. Variation in amplitude and waveform for three upper mantle models for MAST at station HNME.

discontinuity. The HNME seismograms are primarily sensitive to the region below the 600 km discontinuity.

The b and d amplitudes were measured on each seismogram and are listed on Figures 7.2 through 7.4. At the stations within the triplication range (RKON and WH2YK) the ratio of the maximum to minimum amplitudes is about a factor of 2-2.5, though the b phase for HWA-3B at RKON is exceptionally small. Beyond the triplications at HNME, the variation is less, a factor of 1.5-1.6.

The small variation in amplitude at the station beyond the triplications is reassuring. It is, to be sure, based on a limited number of model perturbations, but many of these perturbations were designed to change the amplitude at the HNME range. Any model used must be consistent with the available travel time data, etc., and these data severely constrain the velocity profile. If we assume that parallel layered models adequately represent the upper mantle for our purposes, we can be reasonably certain that errors in our knowledge of the velocity-depth profile lead to errors in our computed amplitudes that are on the order of a factor of 1.5 to 1.6.

If we are within the triplication range, what are the possible variations that occur with small changes in range? Once again, we provide at least a partial answer to the question by showing a typical example. Seismograms for the MAST event were again computed for a series of epicentral distances near that for RKON. The model is HWNE-3. The seismograms together with the b and d amplitudes are shown in Figure 7.5. Over the 67 km range represented the relative amplitudes and arrival times of the incoming rays vary considerably as evidenced by the changing shape of the seismograms. The ratio of the maximum to minimum b and d amplitudes is 1.5 and 1.8, respectively.

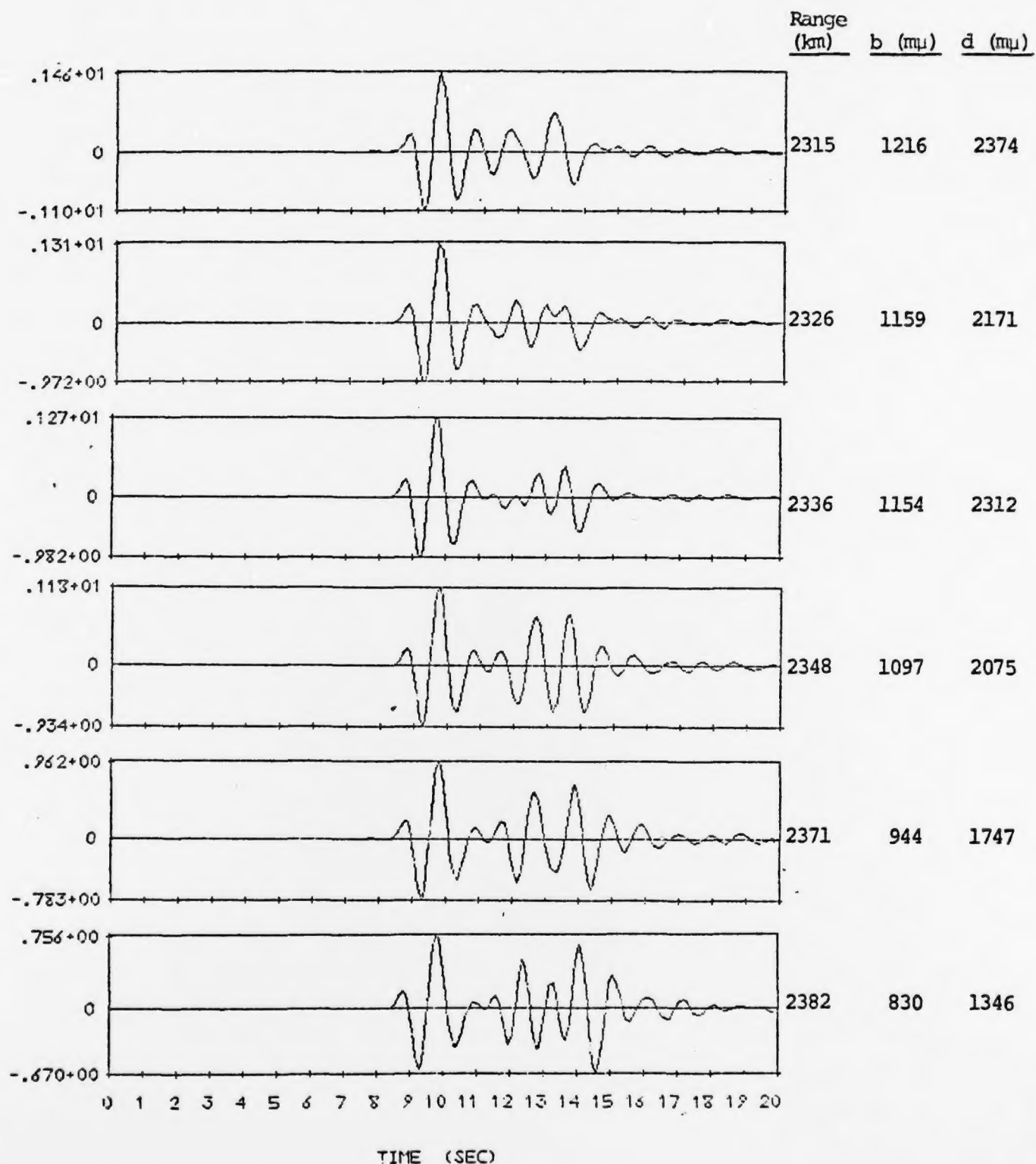


Figure 7.5. Variation in amplitude and waveform with small change in range at station RKON for MAST.

### SUMMARY

Reasonable changes in the elastic properties of the mantle produce changes in P wave amplitude that are on the order of a factor of 1.6 for measurements beyond the triplication distance.

## REFERENCES

- Alewine, R. W., R. W. Klepinger and D. L. Springer (1976), "Teleseismic P-Wave Magnitude-Yield Relations for Well-Coupled Nevada Test Site Explosions," Unpublished Report.
- Anderson, D. L. and R. S. Hart (1976), "An Earth Model Based on Free Oscillations and Body Waves," JGR, 81, 1461-1475.
- Bache, T. C., J. T. Cherry, N. Rimer, J. M. Savino, T. R. Blake, T. G. Barker and D. G. Lambert (1975), "An Explanation of the Relative Amplitudes of the Teleseismic Body Waves Generated by Explosions in Different Test Areas at NTS," Systems, Science and Software Final Contract Report for DNA, October.
- Bache, T. C., T. G. Barker, N. Rimer and J. M. Savino (1976), "Comparison of Theoretical and Observed Body and Surface Waves for Kasserli, An Explosion at NTS," Systems, Science and Software Report SSS-R-76-2937 (Draft), May.
- Bache, T. C. and D. G. Harkrider (1976), "The Body Waves Due to a General Seismic Source in a Layered Earth Model: 1. Formulation of the Theory," Submitted to BSSA.
- Barker, T. G., T. C. Bache, J. T. Cherry, N. Rimer and J. M. Savino (1976), "Prediction and Matching of Teleseismic Ground Motion (Body and Surface Waves) from the NTS Mast Explosion," Systems, Science and Software Report SSS-R-76-2727 (Draft), February.
- Cohen, T. J. (1975), "P<sub>g</sub> and pP Phases from Seven Pahute Mesa Events," BSSA, 65, 1029-1032.
- Fuchs, K. (1966), "The Transfer Functions for P Waves for a Source Consisting of a Point Source in a Layered Medium," BSSA, 56, 75-108.
- Frasier, C. (1972), "Observations of pP in the Short-Period Phases of NTS Explosions Recorded at Norway," Geophys. J., 31, 99-109.
- Haskell, N. A. (1962), "Crustal Reflections of Plane P and SV Waves," JGR, 67, 4751-4767.



Kulhánek, O. (1971), "P-Wave Amplitude Spectra of Nevada Underground Nuclear Explosion," Pure Appl. Geophys., 88, 121-136.

Springer, D. L. (1974), "Secondary Sources of Seismic Waves from Underground Nuclear Explosions," 64, 581-594.

Strick, E. (1970), "A Predicted Pedestal Effect for Pulse Propagation in Constant-Q Solids," Geophysics, 35, 387-403.

Wiggins, R. A. and D. V. Helmberger (1974), "Synthetic Seismogram Computation by Expansion in Generalized Rays," Geophys. J., 37, 73-90.